Monthly Notices
of the
ROYAL ASTRONOMICAL SOCIETY

MNRAS **00,** 1 (2019)
Advance Access publication 2019 August 1

doi:10.1093/mnras/stz2106

The haloes and environments of nearby galaxies (HERON) – I. Imaging, sample characteristics, and envelope diameters

R. Michael Rich [1]★ Aleksandr Mosenkov [2]★ Henry Lee-Saunders,[1] Andreas Koch,[3]★ John Kormendy,[4] Julia Kennefick,[5] Noah Brosch,[6] Laura Sales [7] James Bullock,[8] Andreas Burkert,[9] Michelle Collins [10] Michael Cooper [8] Michael Fusco,[5] David Reitzel,[11] David Thilker [12] Dave G. Milewski [13,14] Lydia Elias,[7] M. L. Saade[1] and Laura De Groot[15]

Affiliations are listed at the end of the paper

Accepted 2019 July 22. Received 2019 June 28; in original form 2018 June 8

ABSTRACT

We use a dedicated 0.7-m telescope to image the haloes of 119 galaxies in the Local Volume to $\mu_r \sim 28$–30 mag arcsec^{-2}. The sample is primarily from the Two Micron All Sky Survey Large Galaxy Atlas (Jarrett et al. 2003) and extended to include nearby dwarf galaxies and more distant giant ellipticals, and spans fully the galaxy colour–magnitude diagram including the blue cloud and red sequence. We present an initial overview, including deep images of our galaxies. Our observations reproduce previously reported low surface brightness structures, including extended plumes in M 51, and a newly discovered tidally extended dwarf galaxy in NGC 7331. Low surface brightness structures, or 'envelopes', exceeding 50 kpc in diameter are found mostly in galaxies with $M_V < -20.5$, and classic interaction signatures are infrequent. Defining a halo diameter at the surface brightness 28 mag arcsec^{-2}, we find that halo diameter is correlated with total galaxy luminosity. Extended signatures of interaction are found throughout the galaxy colour–magnitude diagram without preference for the red or blue sequences, or the green valley. Large envelopes may be found throughout the colour–magnitude diagram with some preference for the bright end of the red sequence. Spiral and S0 galaxies have broadly similar sizes, but ellipticals extend to notably greater diameters, reaching 150 kpc. We propose that the extended envelopes of disc galaxies are dominated by an extension of the disc population rather than by a classical Population II halo.

Key words: galaxies: evolution – galaxies: formation – galaxies: haloes – galaxies: interactions – galaxies: photometry – galaxies: structure.

1 INTRODUCTION

The stellar outskirts or envelopes of galaxies are frequently described using the term 'halo', even though their component stellar populations are unlikely to resemble the Population II stellar population normally associated with the Milky Way halo. These envelopes may range from classical old Population II stars to accreted low luminosity galaxies that may still host star formation and gas. The situation is further complicated by evidence that galactic haloes consist of a mixture of accreted (outer) and *in situ* (inner) components (e.g. Cooper et al. 2013; Pillepich, Madau & Mayer 2015), or metal rich stars related to the spheroid (e.g. Bellazzini et al. 2003). As such, these extended stellar envelopes might consist of ancient halo stars formed *in situ*, debris from an ingested galaxy, relics of stages in the formation of the disc, or stars ejected from the disc of the host galaxy experiencing accretion.

By way of example, deep *Hubble Space Telescope* (*HST*) imaging on the minor axis of M 31 (Brown et al. 2003; Brown et al. 2006) revealed a substantial intermediate-age population. The halo of M 31 is mostly metal rich (Rich et al. 1996; Durrell, Harris & Pritchet 2001; Bellazzini et al. 2003) whilst also hosting both globular clusters, RR Lyrae stars, and a host of substructures in the form of satellites and streams (e.g. McConnachie et al. 2009). Simulations like those of e.g. Mori & Rich (2008) show that a minor merger with a galaxy of mass $M \sim 10^9$ M$_\odot$ can reproduce the many complex structures similar to those seen in the M 31 halo as well as ejecting stars from the disc.

★ E-mail: rmr@astro.ucla.edu (RMR); mosenkovav@gmail.com (AM); Andreas.Koch@uni-heidelberg.de (AK)

Ideally, this study would separate out the different populations of halo stars (*in situ*, accreted, and disturbed disc) using the colours and magnitudes of the stars. However, the age–metallicity degeneracy that affects interpretation of colours and spectra also would affect the stars in the resolved stellar population. As the origins of these structures might be so varied, we must use the term 'haloes' to mean a more complicated type of stellar population than the conventional, e.g. Population II. Recent extensive surveys of interaction signatures of galaxies bear this out; studies by Atkinson, Abraham & Ferguson (2013), Hood et al. (2018), and Morales et al. (2018) report a wide variety of interaction signatures across the galaxy colour–magnitude diagram. These range from organized shells observed around luminous red galaxies, to a huge array of disturbances associated with discs. An examination of the range of interactions raises the question of what the extended structures of galaxies are comprised of, likely a mix of debris from the host and the merger galaxy. For the purposes of our investigation, these low surface brightness structures will be referred to as envelopes, as the term 'halo' might imply a more specific stellar population.

Studies have also shown that the type of envelope a galaxy possesses may relate to its mass. A small survey of galaxy envelope fields from photometric metallicities of resolved stars imaged using *HST* finds an interesting dichotomy, in which galaxies with $M_V < -21$ have relatively metal-rich envelopes (e.g. [Fe/H] $= -0.7$) and lower luminosity envelopes have lower metallicity, closer to -1.5 dex. [Mouhcine et al. 2005; Monachesi et al. 2016; Harmsen et al. 2017]. Although this kind of investigation requires more development, it is important to reflect that more luminous galaxies may have envelopes more related to their central bulges and spheroids, whilst disc galaxies lacking bulges (e.g. NGC 4244) have a more metal-poor envelope. The field of low surface brightness imaging has recently been associated with the discovery of shell structures around elliptical galaxies, spectacular interaction streams, and a zoo of peculiar extensions and structures (e.g. Martínez-Delgado et al. 2010; Duc 2017). Relatively less attention has been paid to investigating the systematics of the quotidian envelopes extending to low surface brightness surrounding galaxies that represent the potentially very long-lived structures. Our investigation explores the correlation of this relaxed envelope diameter with galaxy absolute magnitude, and in this initial study, we explore how envelope diameter varies across the galaxy colour– magnitude diagram.

This paper formally introduces the *Halos and Environments of Nearby Galaxies (HERON)* project, an international collaboration of observers and theorists working to motivate observations of the low surface brightness extensions of galaxies and to compare those results with theory. Future papers will report analysis of quantitative surface brightness profiles, outer envelope morphologies, and other properties including comparisons of extended structures to imaging data at other wavelengths. We will also publish catalogues and luminosities for all low surface brightness candidate companions in the survey. In this project, we build on the heritage of Kormendy & Bahcall (1974) and report envelope diameters to 28 mag arcsec^{-2} for 119 galaxies. Starting in 2019 October, we will begin populating the *HERON* archive at IRSA/IPAC in the community data archives;[1] we will provide data tables, JPEG, and FITS images for the full galaxy sample in the *HERON* survey.

This paper is organized as follows. Section 2 presents our instrumentation, observing strategy, and data reduction. The sample of *HERON* galaxies is introduced in Section 3, along with the measurement of their envelope diameters. In Section 4, we discuss our results, whilst in Section 5, we correlate our results with general galaxy properties, before summarizing in Section 6.

1.1 A brief history of low surface brightness features

The study of low surface brightness galaxy envelopes and extensions has a long history with many interesting subjects; Zwicky (1956) used apertures from the 18-inch Schmidt to the Hale 200-inch telescope, and called attention to tidal tails and extensions of galaxies including NGC 3628. He also emphasized the value of studying such systems by noting the much earlier works of e.g. Pease (1920) and Lundmark (1920). Other early contributions include the career-long work of Karachentsev (1965), which continues to the present day (Karachentsev et al. 2017). Photoelectric photometry exploring the extent of M 87 to a full degree (De Vaucouleurs 1969; Arp & Bertola 1969) was also a remarkably early application of technology to the problem. The analysis of scanned photographic plates of Kormendy & Bahcall (1974) was the first to report a photographic image of the giant stream of NGC 3628 and to report the diameter measurements for a large number of envelopes, some as large as 100 kpc.

Low surface brightness studies returned to the spotlight with the pioneering work of e.g. Malin (1978), Malin (1979), and Malin & Carter (1980). Malin & Hadley (1997) illustrate the remarkable low surface brightness envelopes and streams of spiral galaxies, including a giant arc near M 83. These efforts included the development of 'unsharp masking' and the discovery of low surface brightness shells around elliptical galaxies. Binggeli, Sandage & Tammann (1988) catalogued the Virgo cluster including dwarf galaxies, continued by Ferguson & Sandage (1989). The subject has seen contemporary vitality with the now decades-old explosion of modest aperture telescopes with CCD detectors that have revealed surprisingly extended envelopes of nearby galaxies (e.g. Tal et al. 2009; Martínez-Delgado et al. 2010; Martínez-Delgado et al. 2012; Rich et al. 2012; Van Dokkum et al. 2015; Trujillo & Fliri 2016) and significant work using the Burrell Schmidt Telescope (Mihos et al. 2005; Watkins, Mihos & Harding 2015; Mihos et al. 2017). Duc et al. (2015) undertook low surface brightness imaging of the environs of ATLAS3D[2] ellipticals, updating the Tal et al. (2009) sample, and finding numerous cases of streams, shells, and extended disc star formation. The Pan-Andromeda Archaeological Survey (PandAS) map of the resolved stellar halo of the nearby Andromeda-M 33 complex reveals significant halo structures, demonstrating that the entire extent of the M 31 envelope may stretch halfway to the Milky Way and significantly overlaps with that of the neighbouring spiral M 33 (McConnachie et al. 2009; Ibata et al. 2013; see also Koch et al. 2008). The interesting science questions raised by these analyses have inspired a range of investigations that include networks of small telescopes (Martínez-Delgado et al. 2012), an array of 8 (now 2×24) Canon telephoto camera lenses (the Dragonfly project; Abraham & Van Dokkum 2014; van Dokkum, Abraham & Merritt 2014; Merritt et al. 2016) and our project – the *HERON* survey (Rich et al. 2017).

Any new entry into this subject area faces the long history of research and also serious challenges such as the correct treatment of scattered light (Sandin 2014, 2015). Furthermore, the instrumentation required to enter the field, for the most part, is modest in

[1] www.irsa.ipac.caltech.edu/data/HERON/

[2] www-astro.physics.ox.ac.uk/atlas3d/

cost, enabling numerous individuals and teams to participate. A successful philosophy has been to aggregate very long exposures obtained by citizen scientists with state of the art, commercial off the shelf equipment (e.g. Martínez-Delgado et al. 2010). The Dragonfly array employs commercial technology to minimize scattered light, and builds a powerful instrument from multiple focal planes. An additional relatively recent project is the Purple Mountain 1.0-m Schmidt Near Earth Object Survey Telescope (Shi et al. 2017); this facility has been used to investigate ultra-diffuse galaxies. Special purpose telescopes are under construction and a small space mission has been proposed to undertake imaging at low surface brightness (Muslimov et al. 2017). Serendipitous imaging of galaxy outskirts into resolved stars will also occur as part of the WFIRST mission. In fact, the systematics of Galactic cirrus and scattered light probably, in all likelihood, limit quantitative investigations to the 30–32 mag arcsec^{-2} (in the *r* band) level (for an extreme case of the effects of infrared cirrus, as e.g. for NGC 7743). Pushing fainter than this will require space-based mission that is capable of resolving the low surface brightness structures into stars.

1.2 Theoretical motivation

The low surface brightness envelopes of nearby galaxies offer a unique window into galaxy formation and evolution, and possibly cosmology. These regions hold clues to the hierarchical build-up of structure formation on sub-galactic scales, the very scales where the dominant ΛCDM paradigm is facing its most difficult challenges. Some of the most profound concerns about the ΛCDM theory have arisen in comparison to dwarf satellites and low surface brightness features seen around just two galaxies: the Milky Way and M 31 (Boylan-Kolchin, Bullock & Kaplinghat 2011, 2012). But by relying on just two galaxies of similar luminosity and type we are potentially biasing ourselves significantly. Despite its marked successes in reproducing the large-scale properties of the Universe, the ΛCDM cosmological model faces some significant problems on the mass scales of dwarf galaxies ($M_* \sim M_{\rm vir} = 10^{5-9}$ M$_\odot$). The overall count of dwarfs throughout the Local Group is significantly lower than might naively be expected in ΛCDM-based models of galaxy formation (the 'missing satellites' problem; Klypin et al. 1999; Moore et al. 1999). Moreover, the measured internal mass densities of dwarf satellites are significantly lower than predicted for the ∼10 most massive dark matter haloes near galaxies similar to the Milky Way (the 'too big to fail' problem; Boylan-Kolchin et al. 2011, 2012; Agertz & Kravtsov 2016).

These anomalies do not necessarily mean that our cosmology needs to be revised, as plausible astrophysical solutions have been proposed (e.g. Bullock, Kravtsov & Weinberg 2000; Governato et al. 2010; Di Cintio et al. 2014; Wetzel et al. 2016), but they do strongly motivate the need for alternative tests of the paradigm on the mass scales of dwarf galaxies. One particularly robust test involves looking for tell-tale signs of past dwarf-size merger events around local galaxies: low surface brightness streams, diffuse halo light, and faint heated disc material (Johnston 1998; Bullock, Kravtsov & Weinberg 2001; Bullock & Johnston 2005; Kazantzidis et al. 2008; Cooper et al. 2010; Purcell, Bullock & Kazantzidis 2010; Amorisco 2017). Whilst theoretically well motivated, searches of this kind have been limited largely to resolved-star studies around the Milky Way and M 31 (McConnachie et al. 2009; Belokurov et al. 2006; Belokurov et al. 2007a,b; Bechtol et al. 2015; Cunningham et al. 2016; Mackey et al. 2016). The reason is that the predicted features are extremely low surface brightness, ∼29–30 mag arcsec^{-2}. Until recently, faint features of this kind were prohibitively difficult to detect without resolving them into stars.

Why are low surface brightness features so important? Primarily because the predictions are robust: they rely on the assumption that structure formation is hierarchical down to small scales – one of the fundamental predictions of cold dark matter (CDM) cosmologies. More specifically, if ΛCDM is correct, then galaxy-size dark matter haloes should be built by the steady accretion of smaller, dwarf-size dark matter clumps (e.g. Cole et al. 2000; Stewart et al. 2008; Fakhouri, Ma & Boylan-Kolchin 2010). The rate and timing of these dark matter halo mergers are robustly predicted, at least statistically speaking. Moreover, the stellar content of these dark matter mergers is also well constrained, as the stellar mass of dwarf galaxies needs to drop steeply with decreasing halo mass in a well-defined way to solve the missing satellites problem and (more generally) to explain the observed faint-end of the luminosity function (e.g. Behroozi et al. 2013; Garrison-Kimmel et al. 2017a,b; Read et al. 2017, loosely called 'abundance matching').

The implication is that it should be relatively straightforward to predict the fraction of a galaxy's light contained in diffuse, low surface brightness material as a function of galaxy stellar mass. Purcell et al. (2010) made this point explicitly using a semi-analytic model, and showed that the diffuse light fraction (stellar halo light fraction) should vary strongly with galaxy mass over the galaxy scales of interest here.

2 OBSERVATIONS AND DATA REDUCTION

Our approach to the *HERON* project has been to use and maintain two dedicated telescopes that are proven to reach low levels of surface brightness rapidly, allowing us to upgrade the focal planes, and experiment with different filters and observing modes, all at reasonable cost.

2.1 Instrumentation

We employ the 0.7-m Jeanne Rich Telescope Centurion 28 (C28) at the Polaris Observatory Association site, a dedicated f/3.2 telescope with a prime focus imager behind a Ross doublet corrector, consisting of FS2 and BK7 glass. A conical baffle with ring stops is placed in front of the corrector group to control scattered light. The primary mirror is honeycomb light weighted, and the truss consists of graphite epoxy rods in tension; the optical telescope assembly is supported on an equatorial yoke mount. The control system employs the FS2 astro-electronic telescope control system, by Michael Koch.[3] Focus is achieved using a motor by Robofocus, which focuses by moving the corrector group. The telescope is illustrated in Brosch (2015) and Rich et al. (2017).

The observatory is located in Lockwood Valley, near Frazier Park, CA at an elevation of 1615 m. Although the greater Los Angeles area creates a light dome in the south-east, the site is 21.7–22.0 mag arcsec^{-2} at the zenith and very dark in the West. The manufacturer, James Riffle of AstroWorks Corp in Arizona, produced a number of 0.5-m telescopes of similar design (Brosch et al. 2008) and an identical telescope (the 0.7-m Jay Baum Rich Telescope) operates at Wise Observatory, Israel near Mitzpe Ramon (Brosch 2015; Brosch et al. 2015). A companion project using the Wise 0.7-m Jay Baum Rich Telescope of Tel Aviv University

[3] www.astro-electronic.de/fs2.htm

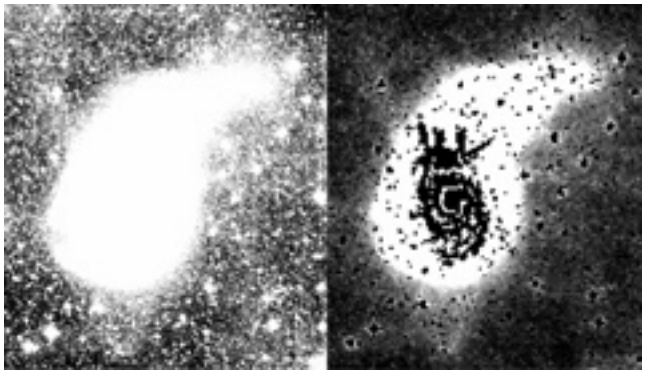

Figure 1. A comparison between our Luminance image of M 51 using the C28 and SBIG11000m imager for 12 × 300 s (left) and *V*-band exposure courtesy of A. Watkins (Watkins et al. 2015) 31 × 1200 s (roughly 10 h) using the 24/36-inch Burrell Schmidt at Kitt Peak (right). Two completely independent approaches to deep imaging are reaching similar depths and revealing similar low surface brightness morphology. This result also addresses concerns that wide angle, faint scattered light might affect our measurements. Both figures show a limiting surface brightness of ∼ 30 mag arcsec^{-2}. The dark inserted feature shows the approximate extent of the higher surface brightness portions of M51. The Burrell Schmidt image has had bright stars subtracted whilst ours has not.

addresses the deep imaging of edge-on disc galaxies and Hickson compact groups and is underway (PI: N. Brosch).

The present image quality is 2.5–3 arsec and poses no impediment to imaging low surface brightness features typically >60 arcsec in size. Remote operations are now routine for the Jeanne Rich C28 telescope. Most of the data set we report on here was obtained using an SBIG STL 11000 CCD that includes a guide CCD alongside the main detector. This camera also has an internal filter wheel that holds 5 round 50 mm filters. The detector is thermoelectrically cooled to typically −25° C; the detector is a KAI1100M interline transfer CCD with 9 μm pixels in a 4008 × 2672 pixel format. The scale is 0.83 arcsec pixel^{-1} with a field of view of 0.57 deg^2. The STL11000m camera has a readout noise of 13e^-, and the A/D conversion (single binned) is 0.8e^-/ADU, and double-binned (a minority of our images) is 1.6e^-/ADU. The FLI09000 used for a subset of our data has 11e^- read noise in the 1MHz readout mode and close to 1.0e^-/ADU. About 20 per cent of our data are double-binned and so indicated. The compact design of this camera with the internal filter wheel results in images with only modest vignetting near the corners. The noise in these images is dominated by the sky background, usually ∼2000 counts, on a given frame.

Since early 2015, we have used an FLI09000 detector on loan from Arizona State University; it is nearly identical to the STL11000m, with a 3056 × 3056 pixel format, lower read noise and 12 μm pix. Guiding for the FLI camera is accomplished via a Lodestar X2 guide CCD mounted on an Astrodon Mega MOAG off-axis guider, in front of the filter wheel. We use a Finger Lakes Instruments CFW2 five position filter wheel that holds 2 inch^2 filters (currently supplied by Astrodon). In order to address some low level image persistence issues, data taken after mid-2016 employs the slow (1 MHz) readout mode using an RBI (Residual Background Image) flood with 400 ms flood time, 4 flushes, and a bin factor of 4, accessed via 'advanced camera settings'.

Although persistence is an issue with the FLI camera, it can be eliminated by using the RBI Flood read mode, which preflashes the imager at the expense of a slight increase in read noise; in any case, nearly all of the data we report here were obtained using the SBIG camera. The FLI Camera operates behind the off-axis guider and filter wheel; this results in greater vignetting than experienced for the STL11000m; however, we are able to flat-field our images successfully and our exposure times overcome the modest loss of light due to vignetting. Our telescope operation and acquisition software is The Sky 6 by Software Bisque and is used for telescope control, Maxim DL version 6 for CCD camera control, and the commercial software Focusmax controlling a robofocus unit, for focus control. Temperature, humidity, sky darkness, and clarity are monitored using a Boltwood cloud sensor from Cyanogen, Ltd.

2.2 Observations and data reduction

The imaging reported in this paper uses a luminance filter, a square bandpass filter from 4000 to 7000 Å with an actual transmission equivalent very approximately to the full Sloan Digital Sky Survey (SDSS; Ahn et al. 2014) *g* and *r* passbands. Its speed enables us to exploit good conditions and to build a large data set rapidly. We calibrate this filter using photometry of stars from the SDSS in the field of our target galaxies; this is described in Rich et al. (2012). We have concluded that the time needed for two-colour integrations is worthwhile only in exceptional cases; the errors in $g - r$ become significant at 25–26 mag arcsec^{-2} (Van Dokkum et al. 2014; Merritt et al. 2016). Our objective is to build a large sample of systems with well-measured stellar envelope luminosities, diameters, morphologies, and satellite properties. A single passband enables these science goals and facilitates follow-up multiwavelength studies if such follow-up appears to be compelling. Figure A1 shows images of the galaxies in our survey; images of all of the galaxies presented here can be found in the electronic version of this article and in the HERON website at IRSA.

We obtain typically 12–36 images of 300s duration for each target. For the case of NGC 128, we measured its diameter for a coadd of three and nine exposures, respectively. We found that the three exposure coadd resulted in a 0.1 arcmin smaller diameter than the nine exposure coadd, which is less than a 3 per cent change, which is smaller than our other sources of error. These are randomly dithered during acquisition by ∼20 arcsec on each move. We attempt to image galaxies near the meridian and avoid results with image quality poorer than 4 arcsec. The MaximDL acquisition software (http://diffractionlimited.com/product/maxim-dl/) includes a guiding control package, and this is employed using the starlight express off-axis guider. As the CCD camera is cooled thermo-electrically only to a temperature ranging from −20 to −40° C, there is still dark current, and we must also acquire dark frames of equal length to the images, at the same temperature as the image frames. These calibrations, along with bias and flat fields, are acquired every few nights. We obtain flat fields frequently, usually every few nights, using the 76 cm square Alnitak XL electroluminescent panel, finding no difference between using the panel and twilight flats. We use an SBIG 340C all sky camera to monitor climate and transparency, and we do not take data in moon or even light cirrus. We verify that the sky is essentially photometric before and during imaging and observations during any moonlight is avoided.

All data are reduced using standard IRAF routines including the subtraction of 300s darks obtained at the same operating temperature as the science frames. In the rare cases where the flat fielding is not optimal, we use the IRAF routine IMSURFIT to arrive at a final flattened background. IMSURFIT fits two-dimensional low order polynomials to the sky background; we limit the polynomial to order <5 and confirm that the application of IMSURFIT does not affect our derived surface brightness profile or measurement

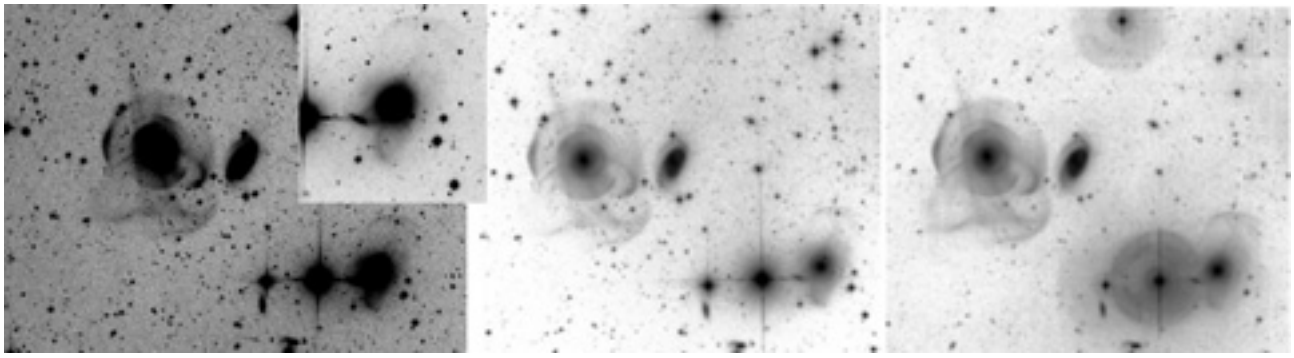

Figure 2. Images of NGC 474 and 470 using different platforms, each showing the faintest features at ∼29 mag arcsec^{-2}. This illustrates our scattered light control; see also the inset of arcs associated with a galaxy interacting with the elliptical galaxy NGC 467. Left: 25 × 300 s exposure (SDSS *g*) using the Jeanne Rich 28-inch telescope. Middle: A 21.5 h exposure using the Irida Observatory 12-inch astrograph; Right: 0.7 h exposure in SDSS *g* using the Canada–France–Hawaii Telescope (middle and right-hand panels from Duc et al. 2015, fig. 7). Notice the scattered light in the three bright images at lower right, and our clean detection of the faint arc.

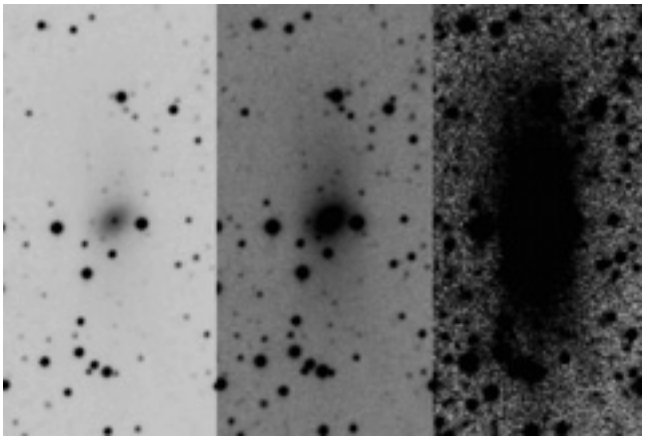

Figure 3. The nucleated dwarf galaxy associated with NGC 7331 at RA 2000: $22^{h}37^{m}12\overset{s}{.}4$, Dec. 2000: $+34°37'12\overset{''}{.}1$. The tidal tails were first reported in Paudel & Ree (2014), where the galaxy is HdE6. N is up and E to the left. The full-frame height is 6 arcmin; the suspected tidal tail feature appears as nearly vertical wings. In this 12 × 300 s exposure, the dwarf is illustrated at three different stretches (compare with fig. 2 of Blauensteiner et al. 2017 from a 26 h exposure). The full extent of the dwarf is 1 × 4 arcmin, corresponding to 4 × 16 kpc at the 14 Mpc distance of NGC 7331. Duc, Cuillandre & Renaud (2018) (their figs 2 and 3) also illustrate this galaxy and show the same extended tails, but do not explicitly mention the galaxy or this structure.

of envelope diameter. It was also very rarely necessary to add a small constant to the frame to avoid oversubtraction. We conclude that our agreement with other studies as evidenced by Figs 1–5 reassures that our instrumentation and reduction procedures reach the standards of other similar studies.

2.3 Surface photometry

The image preparation was done employing a procedure developed by one of the authors (AM) as follows.

An initial step was including astrometry using the website Astrometry.net.[4]

Then we performed photometric calibration using a range of photometric sources. In each frame, isolated, non-saturated stars with a high signal-to-noise ratio were automatically selected (an average number of such stars for all fields was 59). Then we cross-correlated the selected stars with photometric data bases of SDSS, Pan-STARRS (Chambers et al. 2016; Flewelling et al. 2016), and *Gaia* DR2 (Gaia Collaboration et al. 2016, 2018) and transformed their measured magnitudes to the SDSS *r* band using Finkbeiner et al. (2016) and section 5.3.7 from the *Gaia* data release documentation[5] and taking into account Galactic extinction using a 3D dust map from Green et al. (2019).[6] The average calibration error is 0.046 mag. Next, sky was carefully estimated for a sub-field, which includes the target galaxy and some empty background (typically, we use a box with a side five times larger than the galaxy diameter). We use SEXTRACTOR (Bertin & Arnouts 1996) to create a segmentation map for this sub-field and mask out all detected objects. To minimize the impact of the scattered light from the masked objects on the sky fitting, the SEXTRACTOR mask for each object was increased by a factor of 1.5. We then used this mask to fit the sky with a polynomial of some degree, starting from 0 (constant sky level) to 5 (significantly non-linear sky background), increasing this value after each iteration if the sky-subtracted image still had a gradient. Additionally, after subtracting the best-fitting polynomial from the original image, we re-estimated the sky within an elliptical annulus, built around the galaxy on the basis of the preliminary 1D azimuthally averaged profile where the profile flattens (typically, at a radius of the double optical radius R_{25} with an annulus width of 32 pixels). Also, to estimate background variations within the annulus, which can be left after flat-fielding or caused by scattered light from stars, extended objects (satellite galaxies), Galactic cirrus, or low surface brightness features (tidal streams, stellar flows etc.) we determined the variations of the median (using 3σ clipping) inside uniformly located boxes with a side of 32 pixels placed along the annulus. We define the standard deviation of the measured median values within these boxes as the background estimation error. Note that it is different from the standard deviation of the sky level, which is measured for the background within the whole elliptical annulus.

[4] http://nova.astrometry.net/

[5] https://gea.esac.esa.int/archive/documentation/GDR2/

[6] http://argonaut.skymaps.info/

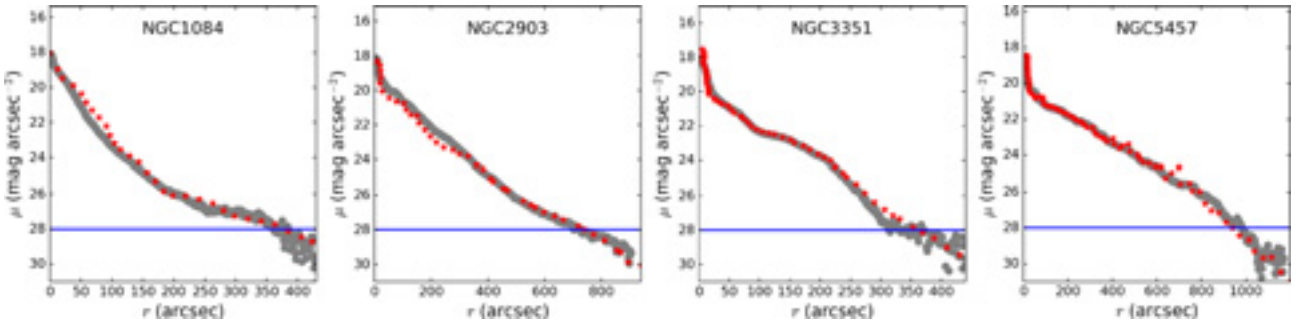

Figure 4. Comparison of our measured surface brightness profiles (grey) for four galaxies from our sample, in common with those observed by Merritt et al. (2016) (extracted from their paper using https://apps.automeris.io). There is excellent agreement between the surface photometry of *HERON* and those of Merritt et al. (2016). Our data reach to $\mu \sim 29$–30 mag arcsec^{-2}. The blue line shows the 28 mag arcsec^{-2} isophote, at which we measure the envelope diameter.

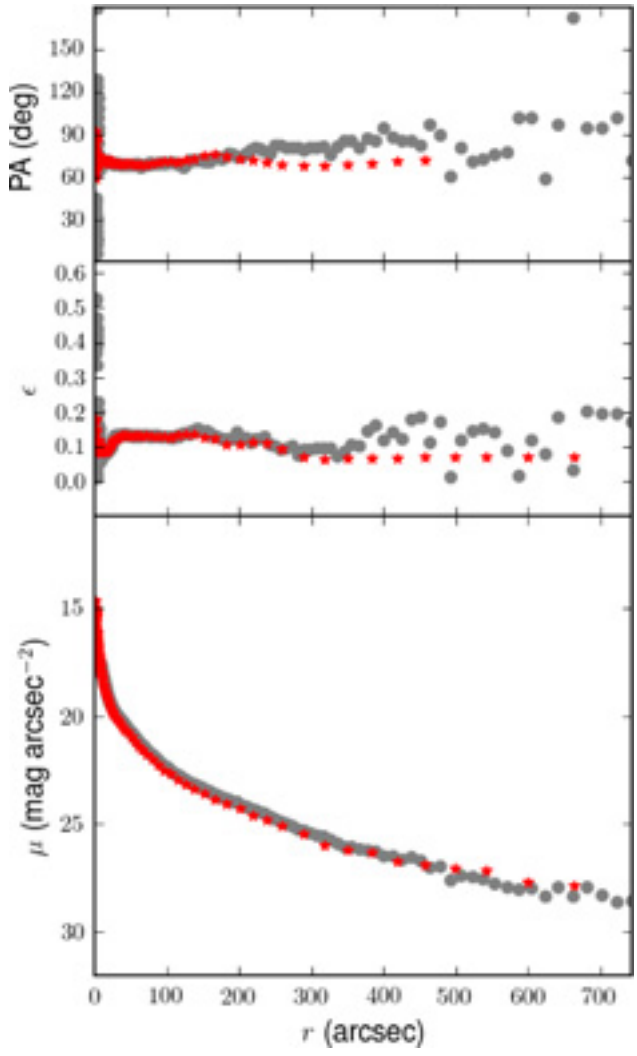

Figure 5. Comparison of our surface brightness profile of NGC 3379 with that of Kormendy et al. (2009) (red stars). *HERON* are data illustrated in grey. Our data reach to $\mu \sim 28.5$ mag arcsec^{-2}.

Finally, galaxy images are cropped to encompass the outermost galaxy isophotes plus some space beyond them (1.5 times larger than the diameter of the outermost isophotes).

To generate surface brightness profiles for a galaxy, we use the following technique. We mask out all foreground stars and other galaxies detected in the final frame. For this, we used the masks, which had been produced earlier, and revisited them by eye. Also, to them we added masks created for the space inside the galaxy by searching for local maxima above the 2D galaxy intensity profile.

For each frame we estimate the point spread function (PSF) for those stars which we used for photometric calibration. Then we perform GALFIT (Peng et al. 2002, 2010) fitting of each galaxy image using a single Sérsic model (Sérsic 1968), convolved with the corresponding PSF. From this modelling, we are able to estimate general parameters of the galaxy position and orientation (position angle) and its ellipticity. We use these values as an initial guess for the IRAF/ELLIPSE routine. We perform isophote fitting starting from the centre and extending up to the outermost isophote which can be detected in the galaxy. The galaxy centre, position angle, and ellipticity in each fit were set free. From the output results of the ellipse fitting we create azimuthally averaged profiles which were corrected for Galactic extinction using Schlafly & Finkbeiner (2011). The profiles will be presented in detail and discussed in a future work, whilst here we only use them to estimate the galaxy diameter (see Section 3.3).

2.4 Scattered light issues and reproducibility of *HERON*

Amateur operated telescopes of professional quality contribute data that reach 29–30 mag arcsec^{-2} in tens of hours of integration (Javanmardi et al. 2016); the 8 lens Dragonfly array attained 32 mag arcsec^{-2} in 35 hours and it is reasonable to assume that a 24 lens array reaches these levels in half the time. Our single detector at the f/3.2 prime focus with a 0.7-m primary is able to detect all of the faint companions reported by Javanmardi et al. (2016), all except the faintest details in M 101 reported in Van Dokkum et al. (2014), and all faint extensions detected in 10 h by the 24/36-inch Burrell Schmidt in M 51 (Watkins et al. 2015; Fig. 1). We also detect all of the streams reported in Miskolczi, Bomans & Dettmar (2011). At the faint levels we work (29–30 mag arcsec^{-2}), it is reasonable to be concerned that wide-angle scattered light might compromise our ability to image and measure faint structures. We have compared our deep images and surface brightness profiles with other work (e.g. Watkins et al. 2015; Fig. 1) and Merritt et al. (2016). These two programmes are, respectively, from the Burrell Schmidt and Dragonfly array, and they report surface photometry to 30 mag arcsec^{-2}. We also note the excellent agreement between low surface brightness details for NGC 4449

and its tidally disrupting dwarf galaxy companion NGC 4449B illustrated in Rich et al. (2012) and Martínez-Delgado et al. (2012). Fig. 2 compares our 12 × 300 s exposure of NGC 474 with a 21 h exposure from the 30-cm astrograph of Irida Observatory[7] and the Canada–France–Hawaii Telescope (CFHT); 0.7 h *g*-band exposure; both of these illustrated in fig. 7 of Duc et al. 2015). An example of the performance attained by our system, reaching ∼29 mag arcsec^{-2}, is shown by the tidal structures revealed in Müller et al. (2019).

Duc et al. (2015) emphasized that the CFHT has serious scattered light haloes not present in the long exposure using the astrograph at Irida Observatory. Our 0.7-m C28 telescope shows exceptionally low scattered light, as good as that of the astrograph and substantially better than the raw CFHT image. The comparison illustrated in our Fig. 2 with that of fig. 11 in Duc et al. (2015) shows that our images can reach at least 29 mag arcsec^{-2} in surface brightness. Whilst not illustrated, our *HERON* imaging of Stephens Quintet reproduces all of the faint structure detected by Duc et al. (2018) also using the CFHT telescope. Significantly, however, Fig. 2 convinces us that our control for scattered light is excellent, reaching or exceeding that of the Irida Observatory astrograph (Duc et al. 2015). Additional comparisons with ∼10 h long images obtained using an 8-inch doublet refractor confirm our excellent scattered light control (B. Megdal, private communication). Example images and comparisons are available on the *HERON* website at IRSA. We will not further discuss the scattered light issue in this paper, as it has no impact on our measurements or conclusions.

Fig. 3 illustrates our image of a dwarf galaxy near NGC 7331. Blauensteiner et al. (2017) published images ranging from 6 to 21 h in depth; however, the tidal tail was actually discovered from SDSS3 images by Paudel & Ree (2014). Here, we are able to discern the full extent of the tidal structure (right panel) reaching 4 arcmin = 16 kpc in total length, making it one of the largest known tidally affected galaxies; our measured size is over a factor of 2 larger than that of Paudel & Ree (2014). We also recover the large tidal tails that can be noted in the CFHT images of Duc et al. (2018) (their figs 2 and 3), but those authors did not explicitly note the object. This tidal feature is twice the extent of NGC 4449B, the tidal dwarf near NGC 4449 (Rich et al. 2012) and is also larger than the dwarf in Koch et al. (2012). We have confidence in our data quality because our low surface brightness features are detected by other investigators using different telescopes and reduction methods. We have not failed to measure any features reported by others in the literature.

In Fig. 4, we illustrate the exceptionally good comparison of our surface brightness profiles with those of four galaxies in Merritt et al. (2016). One galaxy, NGC 4258, is excluded from the comparison as our image does not cover its outskirts, and, hence, our profile is cropped. Table 1 presents our agreement in diameter measurement with Merritt et al. (2016). Fig. 5 compares our surface brightness profile of NGC 3379 with Kormendy et al. (2009) and we attain very good agreement to 28 mag arcsec^{-2}. Note that in Figs 4 and 5 the original profiles from Merritt et al. (2016) and Kormendy et al. (2009) were shifted upwards to match the inner part of our profiles (excluding the very centre where our observations can be saturated), as their observations were done in the *g* and *V* band, respectively.

In Section 3.3.1, we consider the impact of the extended PSF on the measured diameters.

[7] www.irida-observatory.org/

Table 1. Envelope diameter comparisons between the *HERON* measurements (at the level of 28 mag arcsec^{-2}) and those from Merritt et al. (2016). We only compared galaxies that were in both samples, except for NGC 4258 (see the text). The radii were measured on the basis of Fig. 4.

NGC	*HERON* diameter (kpc)	Merritt et al. diameter (kpc)
1084	27.2	28.0
2903	32.6	33.5
3351	16.9	17.4
M 101	33.8	32.5

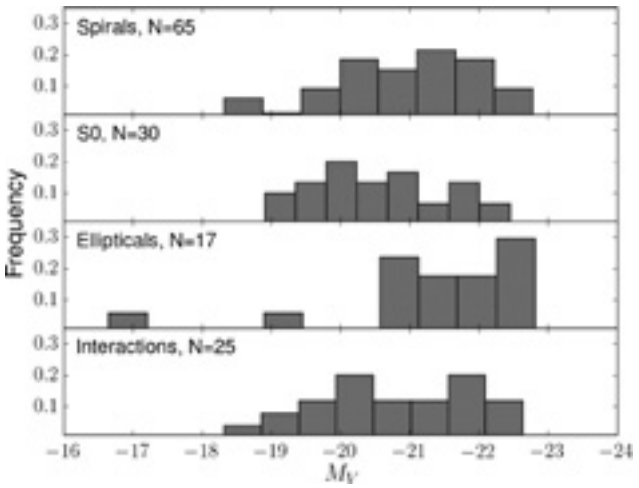

Figure 6. The *V*-band absolute magnitude (M_V) distribution for the *HERON* sample, divided by Hubble type. The sample labelled as 'interactions' represent the subset of our sample displaying interaction signatures such as streams and arcs outside of the main galaxy body.

3 ANALYSIS

3.1 Sample

Most of our galaxies were selected from the Two Micron All Sky Survey (2MASS) Large Galaxy Atlas (Jarrett et al. 2003). We also observed a smaller sample of nearby low luminosity galaxies selected to have large angular diameters from the Karachentsev et al. (2017) catalogue, and with more distant early-type galaxies from the ATLAS3D survey.

Whilst *HERON* is by no means intended to be a volume-complete survey, we note that our sample encompasses ∼1 per cent of the galaxies in the Local Volume within 50 Mpc, given in White, Daw & Dhillon (2011).

Fig. 6 shows the distribution of absolute magnitudes of our final sample, sorted by Hubble type. Although our sample has a large number of relatively nearby galaxies, it is dominated by galaxies with $M_V < -20$. We are addressing that shortcoming by observing low-luminosity galaxies selected from the Karachentsev et al. (2017) catalogue.

3.2 Depth of the images

Based on the created averaged surface brightness profiles (see Section 2.3), we determined a limiting surface brightness level for each sample galaxy where the error of the intensity is comparable to its value. These values are listed in Table B2.

Fig. 7 shows a histogram of the limiting surface brightness levels.

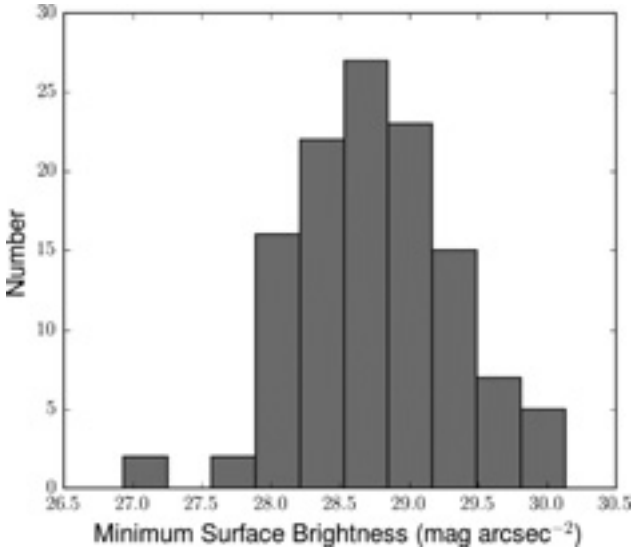

Figure 7. Histogram displaying the corresponding surface brightness that our diameter measurements reached. The histogram displays a mean value of 28.8 mag arcsec^{-2} and a standard deviation of 0.5 mag arcsec^{-2}.

The distribution looks normal with a mean surface brightness of $\sim$28.8 $\pm$ 0.5 mag arcsec^{-2}. 115 galaxies (97 per cent) have limiting diameters at surface brightness levels deeper than 28 mag arcsec^{-2} and 37 (31 per cent) deeper than 29 mag arcsec^{-2}. It appeared that four galaxy images in our sample (NGC 525, NGC 4258, NGC 7465, and UGC 4872) do not demonstrate deep profiles (their limiting surface brightness is higher than 28 mag arcsec^{-2}). Therefore, we do not consider them in our further analysis.

As the vast majority of our sample galaxies have surface brightness profiles that extend to 28 mag arcsec^{-2} and deeper, we decided to define the diameter of the envelope/halo at this level. Further, we will refer to it as the envelope diameter. Alternatively, we will use the envelope radius as half the envelope diameter.

3.3 Diameter measurements and magnitudes

We find that one of the most reliable and reproducible features is the measurement of the diameter as determined at a fixed surface brightness level. As defined above (see Section 3.2), the envelope diameter (radius) is measured at the 28 mag arcsec^{-2} isophote, as almost all galaxies in our sample have surface brightness deepness up to this isophote. As some systematic errors may potentially influence the measured diameter, such as the uncertainty of the background measurement, the calibration error, the local error of the IRAF/ELLIPSE model, we used Monte Carlo simulations to model galaxy profiles with taking into account all these errors. This allowed us to estimate an error on the diameter. We calculated that an average error of the envelope diameter for the whole sample is 3.4 $\pm$ 1.6 per cent of the diameter value. In Table B3, we provide the diameter values and its errors, along with the envelope shape that was visually estimated for each galaxy. We are about to discuss these envelope shapes in our subsequent study.

An example of a diameter measurement at two surface brightness levels, 28 and 29.4 mag arcsec^{-2} (the limiting surface brightness level for this galaxy), are illustrated in Figs 8 and 9.

In order to report a physical diameter and absolute magnitude, we must adopt a distance. In this work, we use the redshift-independent distances provided by the HyperLEDA data base[8] (Makarov et al. 2014). For galaxies without redshift-independent HyperLEDA distances, we use the redshift-independent distances provided by the NASA/IPAC Extragalactic Database (NED)[9] or the flow-corrected redshift-derived values provided by NED (if no redshift-independent distances are provided).

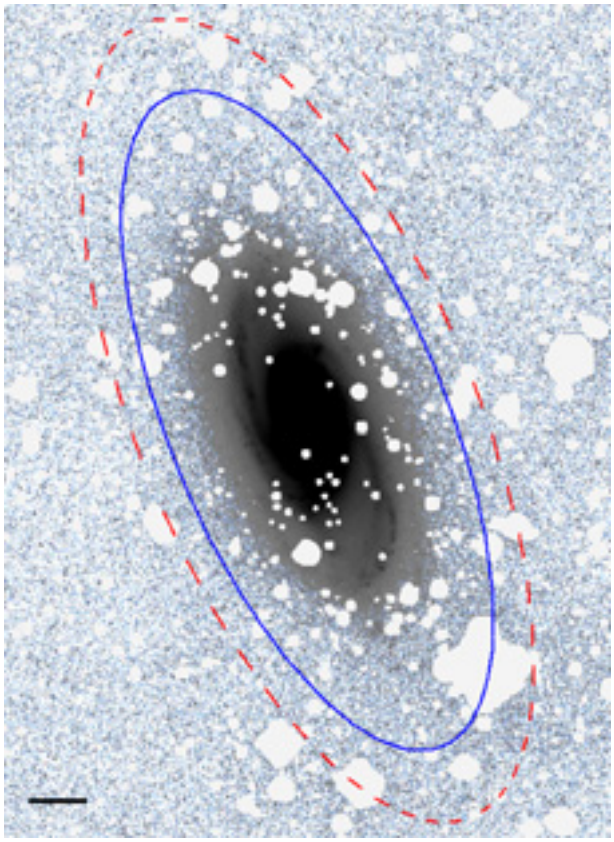

Figure 8. This figure displays two envelope diameters for the SABbc galaxy NGC 2903 (see also Merritt et al. 2016). The blue solid ellipse is related to the isophote 28 mag arcsec^{-2}, whereas the red dashed ellipse to the 29 mag arcsec^{-2}. NGC 2903 has a diameter of 24.1 $\pm$ 0.6 kpc at M_V = $-$21.57. This figure is intended to display the lowest surface brightness we reached; other images with scale bars are shown in Appendix A (Fig. A1). The scale bar in the left bottom corner shows 2 arcmin.

As some of our galaxies may have saturated nuclear regions, we do not use our photometry to measure galaxy fluxes. Instead, we adopt from HyperLeda the magnitudes m_V and the colours $B - V$, denoted as *btc* and *bvtc*. These have been corrected for Galactic extinction using Schlafly & Finkbeiner (2011) and internal absorption (see comments in HyperLeda).

3.3.1 *Impact of the PSF on our measurements of the diameter*

As the PSF can significantly affect the real galaxy profile (see e.g. Sandin 2014, 2015), we need to ensure that our measurements of the diameters do not suffer from this effect. For this purpose, we should use an extended PSF, where extended wings should be larger than 1.5 times the distance between the outermost galaxy isophote (in our case, it is 28 mag arcsec^{-2}) and the centre, where we usually observe

[8] http://leda.univ-lyon1.fr/
[9] https://ned.ipac.caltech.edu/

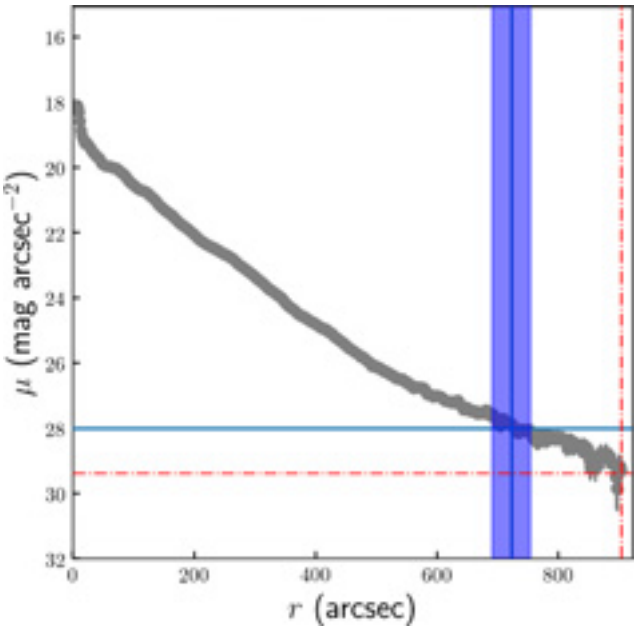

Figure 9. Example of the envelope radius measurement for NGC 2903. The blue solid horizontal line shows the surface brightness level 28 mag arcsec^{-2}, whereas the red dot–dashed horizontal line shows the limiting surface brightness level for this galaxy (29.4 mag arcsec^{-2}). The vertical lines show a measure of the envelope radii at these levels. The blue stripe for the radius of the 28 mag arcsec^{-2} isophote includes different systematic errors (see the text).

the maximum intensity. To take into account the PSF effect, two approaches are used. The first method includes a multicomponent modelling of the galaxy using the convolution with an extended PSF (Trujillo & Fliri 2016). The second approach uses deconvolution techniques (see e.g. Karabal et al. 2017). As our sample consists of a rather large number of objects of different orientation, morphology and angular size, the first approach is extremely time-consuming. The second approach is more promising, taking into account a constantly increasing computational power to solve such kind of problems. This work has to be done in the future.

In this study, we decided to investigate the effect of an extended PSF on our galaxy profiles by performing simulations of galaxy images and then convolving them with the extended PSF.

To create an extended PSF for the *HERON*, we use an observation of the bright star HD 9562. Using the IRAF/ELLIPSE routine, we created its azimuthally averaged profile up to a radius of ≈1000 arcsec. However, as its central part is saturated, we replace the core of the extracted profile by a non-saturated star (the normalization was done at the intersection of the profiles, see Karabal et al. 2017 for details). The synthesized profile is shown in Fig. 10.

As in our sample there is a large variety of morphologies, let us consider three simple models of galaxies: with the Sérsic index $n = 1$ (late-type galaxy), 2 (galaxy with a compact bulge), and 4 (elliptical galaxy). Other parameters of the Sérsic model are the effective radius, 47 arcsec and the effective surface brightness is 21.2 mag arcsec $^{-2}$ (these are the average values for our sample determined from our GALFIT decomposition, see Section 2.3). The 2D images were simulated with GALFIT and then convolved with the extended *HERON* PSF. The results of the envelope radius estimation are shown in Fig. 11. As one can see, the overestimation of the real radius at the 28 mag arcsec^{-2} isophote is very small (less than 1.5 per cent for all n). However, it is getting larger for lower surface

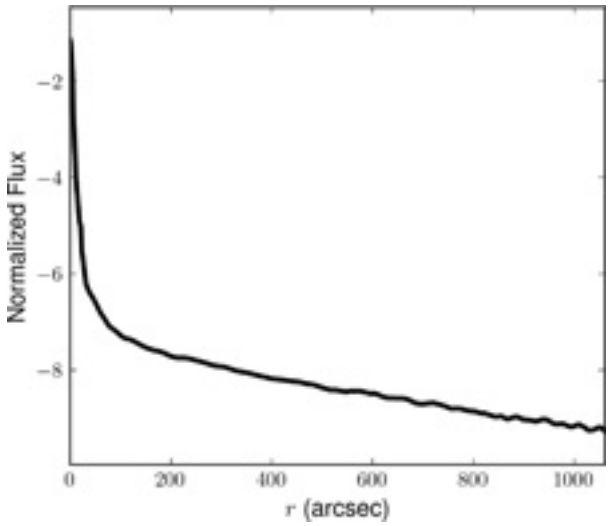

Figure 10. Normalized azimuthally averaged profile of the PSF model profile.

brightnesses: for the 30 mag arcsec^{-2} isophote an overestimation increases up to 5.5 per cent for $n = 1$. From this comparison, it is obvious that our measurements of the envelope radius are within the typical errors of the envelope radius, and cannot affect our results. We should notice, however, that the presence of an AGN may change this conclusion, as the bright compact source will produce extended wings that can be mis-interpreted as a halo. However, only 12 galaxies in our sample exhibit some activity at the centre; therefore, we do not consider this case.

3.3.2 Tests of our diameter measurement metric

In order to reassure us that our measurement of diameters is robust and does not arise due to a selection effect, we have performed a number of tests on the data.

Fig. 12 shows that there is no correlation between diameter and apparent *V* magnitude. If scattered light from bright central bulges or discs were a significant contributor to our measurement of diameter, one might expect to see a correlation between diameter and apparent magnitude. Fig. 13 presents our correlation between diameter and radial velocity. Again, no strong correlation is expected. However, our most distant galaxies include some of our most luminous. Fig. 14 considers absolute magnitude versus radial velocity. Our sample is under represented at the faint end; as mentioned previously, we are taking steps to address this. We conclude from these tests that our measurements of diameter do not suffer from any systematic trends, and they do not behave as expected if the diameter measurements were seriously affected by scattered light or systematic error.

4 DISCUSSION

We now address how our measurement of envelope diameter correlates with various physical properties of galaxies in our sample. We first consider the characteristics of our sample as a whole in Fig. 15. S0 and spiral galaxies span the widest range in luminosity. Although our most luminous galaxies are elliptical, the absolute magnitude distribution of galaxies by Hubble type and presence of interaction signatures is remarkably similar.

Fig. 15 shows a strong primary correlation between the measured physical diameter of the envelope, and absolute *V* magnitude,

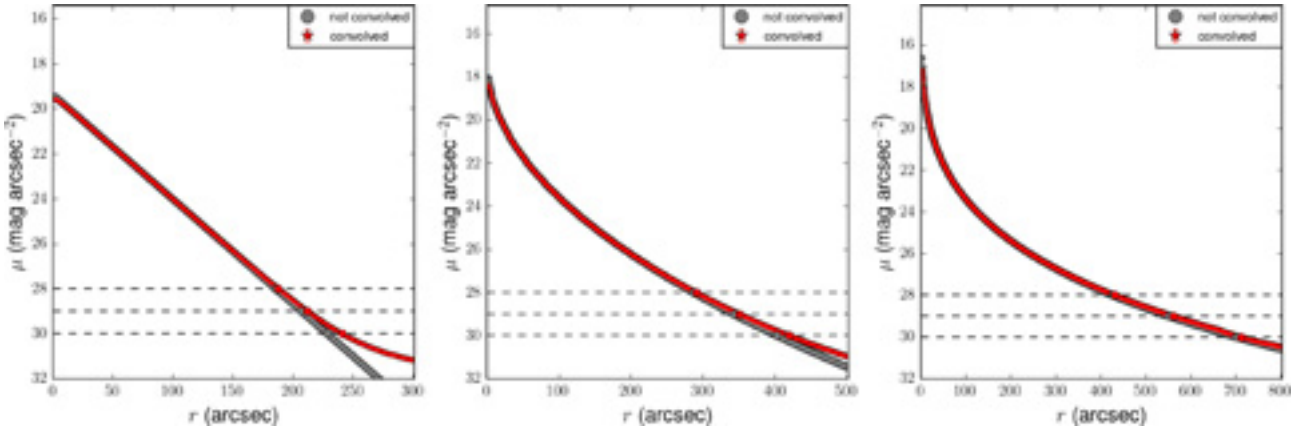

Figure 11. The comparison of the original (non-convolved) and convolved profiles for three Sérsic models with $n = 1$ (left), $n = 2$ (middle,) and $n = 4$ (right). The dashed lines show some characteristic surface brightness levels of 28, 29, and 30 mag arcsec^{-2}.

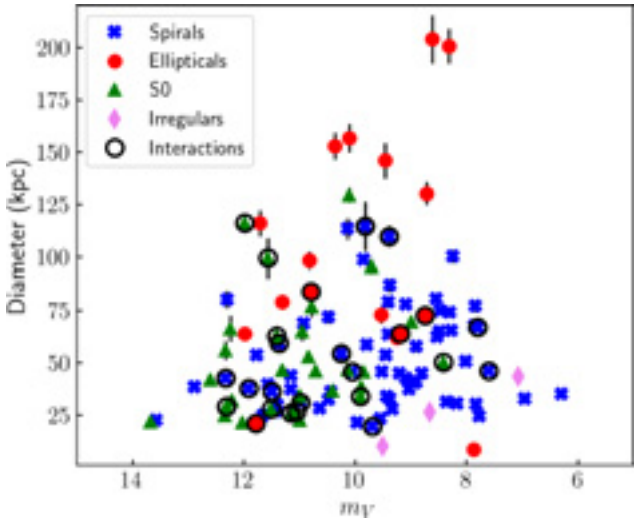

Figure 12. Envelope diameter (kpc) versus apparent V magnitude. We do not see any trend, as expected if scattered light does not contribute to the measured envelope diameter. The apparently brightest galaxies might in principle have spuriously larger diameters caused by scattered light from their e.g. bulge or disc components.

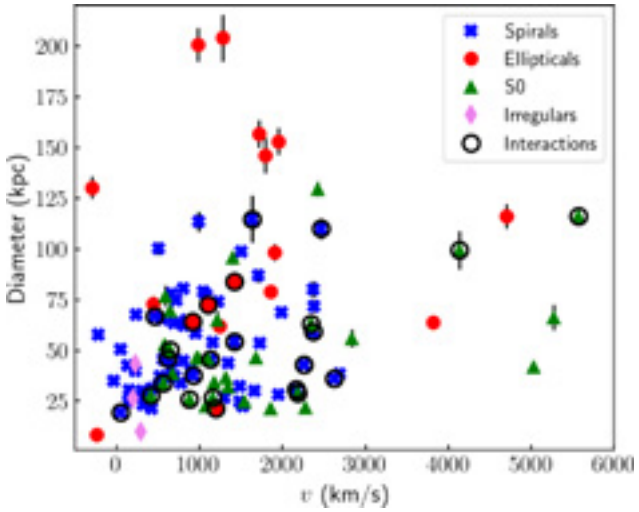

Figure 13. Envelope diameter (kpc) versus radial velocity with galaxy classification indicated. No trend is evident; the distant galaxies with large haloes correspond to luminous systems that are more rare in our lower redshift sample. The lack of any strong correlation of halo diameter with velocity is expected.

agreeing with our work earlier reported in Rich et al. (2017). We have confirmed this trend based on diameters at 25 mag arcsec^{-2} (D25) from the NED Data base. The D25 data confirm the general trend, but as expected, do not reach the largest diameters. Similarly, our work confirms the work of Muñoz-Mateos et al. (2015) that finds similar trends in galaxy diameter and stellar mass from *Spitzer* data. Our data show an apparent transition near $M_V \sim -20.5$ or L^* at which point a subset of galaxies, mostly E and S0, begin to display very large diameters, reaching 150 kpc. However, a few spirals also have large envelopes, as previously noted by Kormendy & Bahcall (1974). We find no tendency for interactions to be detected in a particular magnitude range, except for their relative paucity for $M_V > -20.5$. This trend is not a simple correlation between galaxy diameter and total mass. For example, at $-20 < M_V < -24$, galaxies of all morphological types exhibit a total range in measured diameter from 20 to 170 kpc and within this most luminous category there is only weak dependence of diameter on luminosity.

When plotted as log diameter versus stellar mass in Fig. 16, the apparent break at L^* is not as evident; we also observe a trend similar to that found by Muñoz-Mateos et al. (2015). This plot also suggests that ∼200 kpc may represent an upper limit to envelope diameter, although more observations are required to confirm this. One very large envelope with diameter ∼170 kpc has been found surrounding Hickson group HCG 98 and is reported in Brosch et al. (2019). It will be important to explore whether these correlations extend to the total luminosities encompassed in small galaxy groups.

4.1 The galaxy colour–magnitude diagram

We turn next to explore correlations across the galaxy colour–magnitude diagram. Our motivation is to explore whether the signatures of active interactions preferentially populate any part of the CMD. Fig. 17 shows that galaxies hosting interaction signatures (Duc 2017) appear to show no preference for populating the blue or red sequence, or the green valley. Interactions may be a significant factor in driving quenching, as the significant infall of baryons and dark matter might be expected to be a factor that induces star formation.

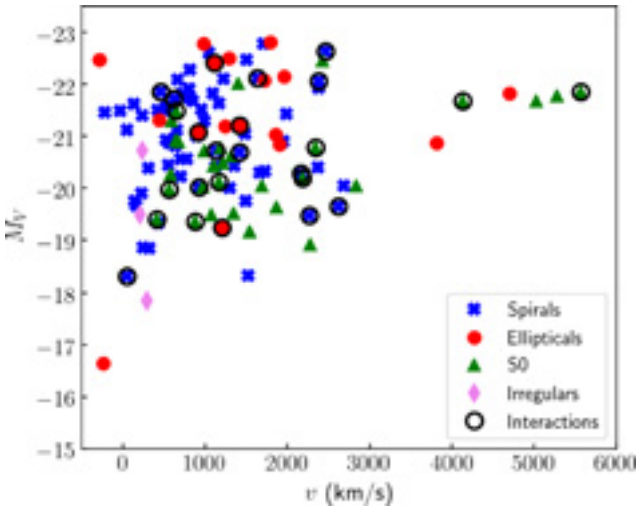

Figure 14. A plot of absolute V magnitude (M_V) versus radial velocity. The sampling in absolute magnitude and radial velocity shows no apparent bias. The present sample is relatively sparse at the low luminosity end; this will be supplemented using the Karachentsev et al. (2017) catalogue, as described in the text.

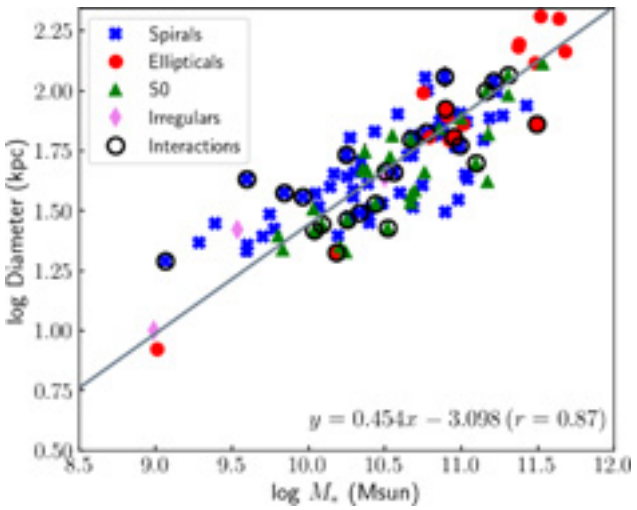

Figure 16. Log diameter in kpc versus stellar mass using the relationship of Bell et al. (2003). The trend extends to lower surface brightness that reported in Muñoz-Mateos et al. (2015).

Fig. 18 shows a new result: the largest envelopes appear to preferentially populate the luminous end of the red sequence and include both S0 and E galaxies. However, large haloes are also seen in the blue cloud. We previously found that the envelope size is correlated with luminosity and recall that Fig. 20 shows that elliptical galaxies host the largest haloes; hence, the largest envelopes are found in $M_V < -21$ galaxies on the red sequence.

However, the largest envelopes are not *confined* to the red sequence, with the most luminous blue sequence members and at least one green valley galaxy exhibiting large envelopes as well. It will be interesting to consider the role of environment in future work; however, it is noteworthy that only the bright end of the red sequence hosts the largest envelopes. There appears to be no clear preference for larger envelopes on the faint end of the red sequence compared to the blue cloud. The strong primary correlation between intrinsic luminosity and envelope size is of greatest importance, but for galaxies with $M_V < -21$, the envelopes of greatest diameter are found at the bright end of the red sequence and are notably less common in the blue cloud and green valley. Simulations also predict, at fixed stellar mass, more massive stellar haloes in red galaxies than in blue (Elias et al. 2018). However, as noted originally

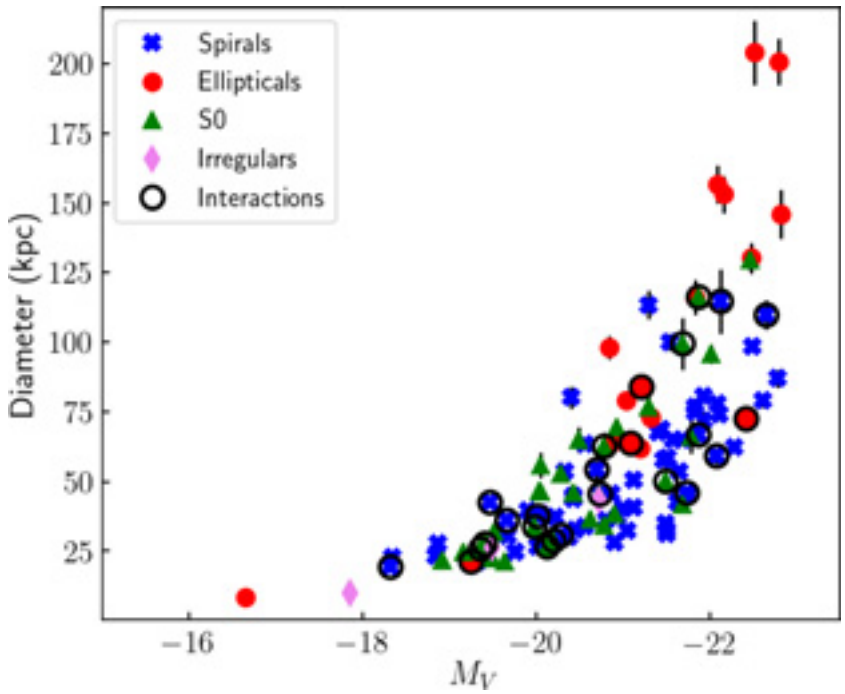

Figure 15. A plot of envelope diameter (kpc) versus absolute magnitude M_V. Galaxy classification is according the symbols in the legend. Circled symbols indicate galaxies with a stream, extended shell, or otherwise strongly asymmetric interaction. The largest envelopes are found in the most luminous galaxies.

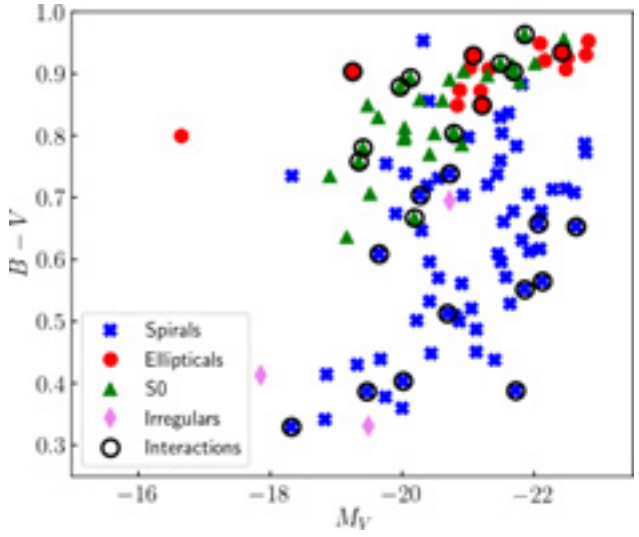

Figure 17. A plot of $B - V$ colour versus M_V. Circled symbols indicate interactions. The diagram divides cleanly into the luminous red sequence, green valley, and blue cloud. Interactions appear to occur throughout this plot and do not favour a particular location.

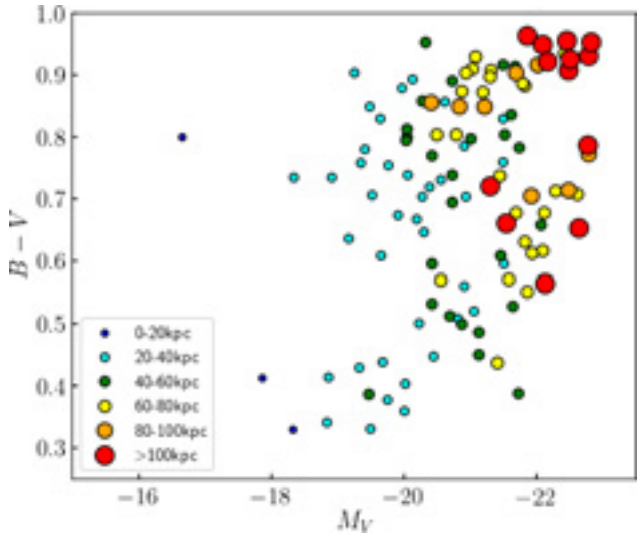

Figure 18. The same plot as Fig. 17, $B - V$ colour magnitude versus M_V. Here, the different coloured symbols represent different envelope diameters according to the legend. The bright end of the red sequence hosts the largest envelopes, those with diameter >100 kpc, but the faint end of the red sequence has halo sizes comparable to that of the blue cloud. The largest envelopes are seen in the most luminous galaxies regardless of whether they occupy the blue cloud, green valley, or red sequence. Envelopes of median diameter can be found across the plot.

by Kormendy & Bahcall (1974), the largest envelopes can be found in both spirals and ellipticals.

The cases of very large envelopes not on the red sequence are unusual. NGC 474 is an elliptical galaxy in the green valley, but it is involved with a significant (likely recent disc) merger event. The merger shells are bluish on false colour images (see e.g. Duc et al. 2015); this galaxy will likely migrate to the red sequence after the merger event settles. NGC 5746 shows one of the largest envelopes found for a galaxy in the blue cloud. This edge-on, boxy/peanut-shaped bulge galaxy has an extraordinary 60.3 kpc

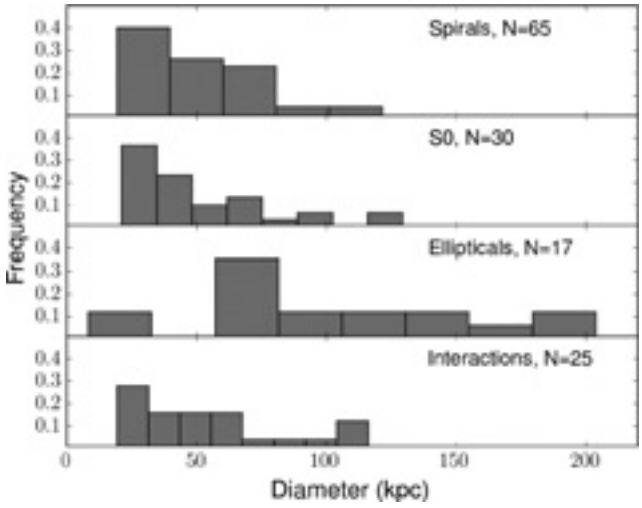

Figure 19. A set of histograms displaying the number of galaxies as a function of envelope diameter (kpc), separated by Hubble type. We can see that spiral and S0 galaxies are, in general, smaller than elliptical galaxies in our sample. The 'interactions' histogram displays the envelope diameters of galaxies in our sample that show signs of interaction; such features include streams, plumes, or shells.

diameter envelope, and its rotation curve has the highest peak velocity in the Bureau & Freeman (1999) sample; ±500 km s^{-1}. NGC 772 is also identified as being in the blue cloud, but it is a face-on spiral with one spiral arm and 3 galaxies entrained in a stream; they all lie projected on a field of complex infrared cirrus. It is in the blue cloud by virtue of its disc, and hosts an extremely large envelope due to the ongoing interaction. NGC 474, NGC 772, and NGC 5746 are anomalous in their hosting of large envelopes yet not residing on the red sequence. The remaining largest envelopes clearly reside on the red sequence and are ellipticals and S0s.

In Fig. 19, we note that the largest envelopes are found in elliptical galaxies, but that galaxies with interactions host envelopes that span the full range of diameter. Larger samples will be required to assess whether interactions are found in specific circumstances e.g. small groups or close companions. Future work will also address low-luminosity companions and their characteristics.

Fig. 20 shows the very clear difference in the distribution of envelope diameters when segregated by luminosity. It is clear that the bulk of galaxies with $M_V < -20.5$ have envelopes larger than those fainter, a statistic that is highly unlikely to change, even if the sample size were to increase. In Fig. 21, we present the histograms that correspond to an approximate red sequence/blue cloud colour cut in Fig. 18; this reinforces our claim that the largest haloes are found on the red sequence.

5 THE NATURE OF ENVELOPES OF DISC GALAXIES

In Fig. 22, we ask whether projected orientation has an impact on the measured diameter of the envelope. We find no indication for differences in the diameters of face-on compared to edge-on disks. We now turn to consider the possibility that the outermost detected light in face-on discs (e.g. Merritt et al. 2016) may arise from a disc population, and may not be a classical Population II halo.

The outer edges of spiral galaxies are broadly observed to divide between those showing evidence of star formation and spiral or flocculent spiral structure (e.g. M 101) and those showing a smooth

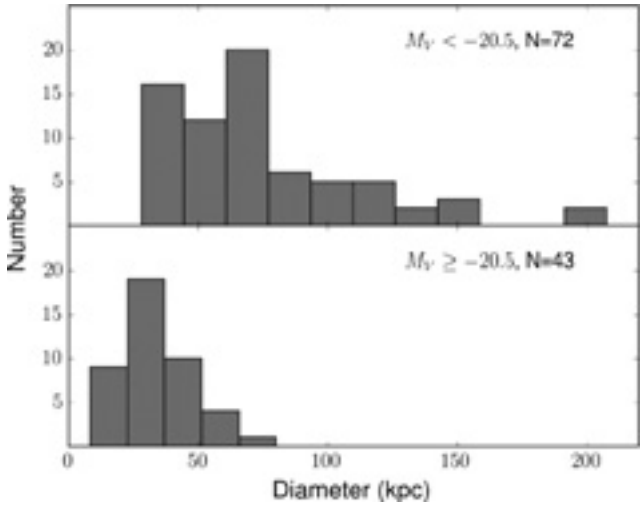

Figure 20. Histograms displaying the number of galaxies as a function of envelope diameter (kpc), divided by absolute magnitude at $M_V = -20.5$. It is clear that galaxies with $M_V < -20.5$ have a greater envelope diameter.

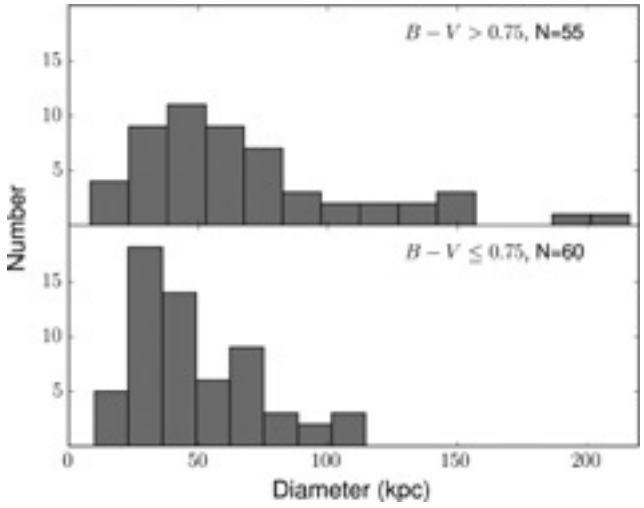

Figure 21. Another illustration that the largest haloes are found at the bright end of the red sequence (Fig. 18). Histograms displaying the number of galaxies as a function of envelope diameter (kpc), divided by colour at $B - V = 0.75$. This represents a rough colour cut between the red sequence and blue cloud.

outer extension (M 83). Fig. 23 illustrates these examples; they represent extremes, with star formation at the outer edges being the more common occurrence. M 51 presents a smooth but unusually shaped outer envelope, whereas M 74 and M 101 appear to show the more commonly seen spiral structure. In the case of M 83, the outer envelope is unusual in that it extends substantially beyond the disc, shows no spiral structure even in subtraction, and is oval and off-centred. This outermost structural feature suggests that (as is the case with M 51) its envelope is more likely to be a flattened disc-like projection.

Exploring further the question of which stellar population is represented in the outer parts of spirals, we present subtractions of the ELLIPSE models for galaxies that are discussed in Merritt et al. (2016). In Fig. 23, we can observe that the outer regions of NGC 1084, NGC 3351, and NGC 2903 show clear spiral structure in subtraction. Using both imaging from the 0.7-m C28 telescope

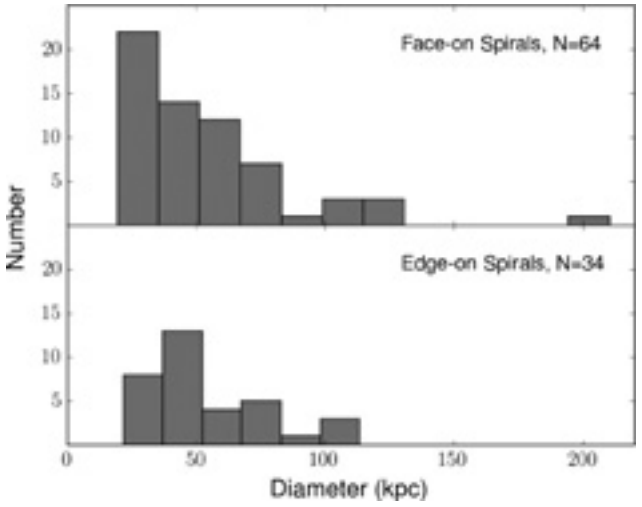

Figure 22. Envelope diameter for face-on and edge-on spirals. The KS-test gives $\mathcal{D} = 0.15$ and a p-value $\mathcal{P} = 0.62$ for this result. We do not find strong evidence for different diameters for edge-on versus face-on discs.

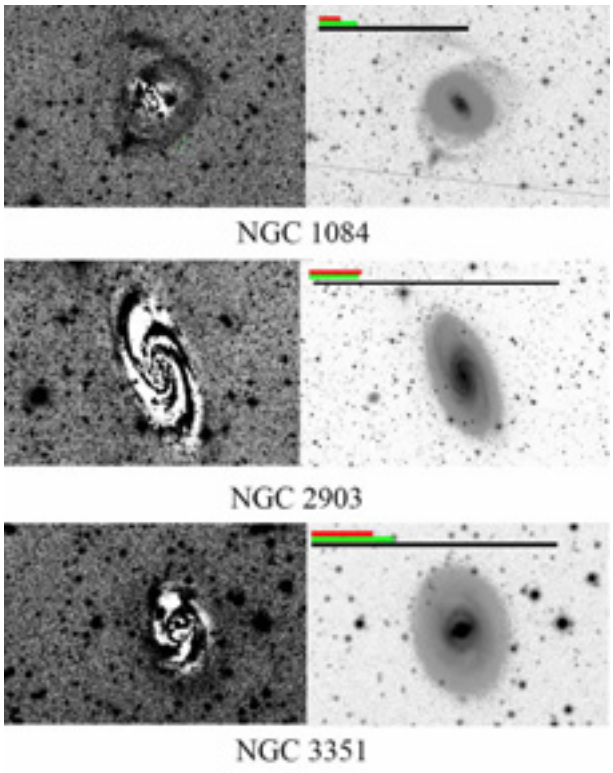

Figure 23. Subtraction images next to the corresponding inverse image. The black scale bar on the inverse image panels represents the diameter at the 30th mag arcsec^{-2} that Merritt et al. (2016) lists in their paper. The green bar represents 5 arcmin and the red bar represents 10 kpc.

as well as verification images obtained by B. Megdal employing a single lens 8-inch refractor (to reduce scattered light issues), we do not detect envelope light outside of the extreme edge of the disturbed disc (the broad 'arm' like structure at the top of the NGC 1084 image in Fig. 23). The refractor observations were undertaken in order to confirm that our 0.7-m data are not compromised by scattered light. Our images do not present the extended low surface brightness

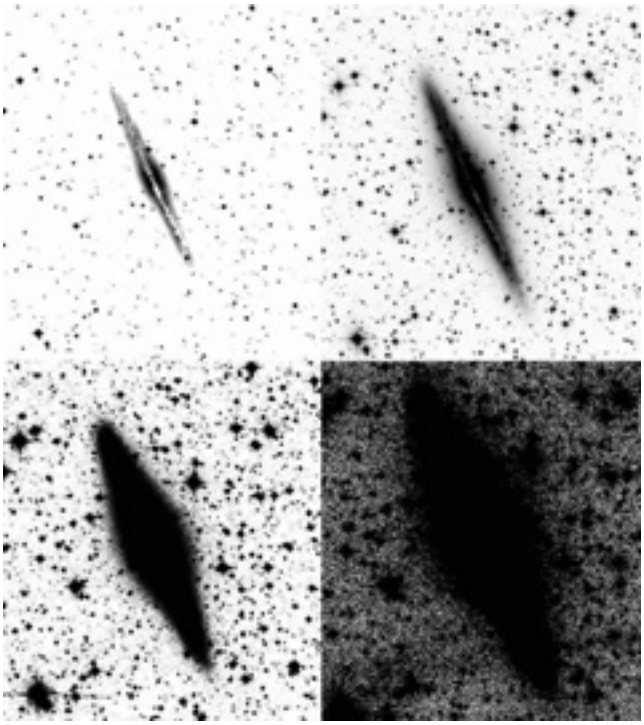

Figure 24. The edge-on spiral galaxy NGC 891 is displayed from shallow to deep stretch. Notice that the minor axis of the bulge is significantly smaller than the extent of the disc major axis; this is typical of all edge-on disc galaxies. At the deepest stretch, the galaxy assumes a 'trapezoidal' appearance due to the extent of the spheroid, but the disc always has the greatest major axis.

profiles reported in Merritt et al. (2016) but our surface brightness profiles appear to show similar extent as illustrated in Fig. 4.

Finally, Fig. A1 in the Appendix present images of galaxies included in our study, along with scale bars for apparent and physical diameter. The entire set of images, including additional galaxies not included in this paper, will also be made available in the *HERON* archive at IRSA.

Noting that a significant fraction of edge-on disc galaxies exhibit disturbances (e.g. NGC 3628 and NGC 4216), we suspect that the faintest detectable light at the edges of face-on discs in disc galaxies should be attributed to the disc, not the halo. Fig. 24 illustrates NGC 891, a typical edge-on galaxy with a bulge. The deepest exposures show that the outermost isophotes are trapezoidal, with the major axis aligned with the disc. Amongst the most striking examples of an edge-on trapezoidal envelope is NGC 2683. The minor axis is always aligned with the spheroidal component and perpendicular to the disc. This is characteristic of all of our edge-on disc galaxies: we have no cases where a low surface brightness envelope ever projects to a larger size than the disc, save for that of M104. M104 can be considered a disc galaxy, showing a prominent dust lane and bulge, but does show one of the largest haloes (extended spheroid) in our sample.

Fig. 25 shows the unusual case of NGC 3628. Although the tidal tail has long been noted, the buckled and disturbed disc is thick, with the deepest isophotes showing a boxy 2:1 structure. One could safely assume that all light contributing to the low surface brightness components of this galaxy belongs to the disc. Fig. 26 shows the disturbed edge-on S0 galaxy NGC 4762. Deep images have previously shown the disturbed disc in the second panel, but

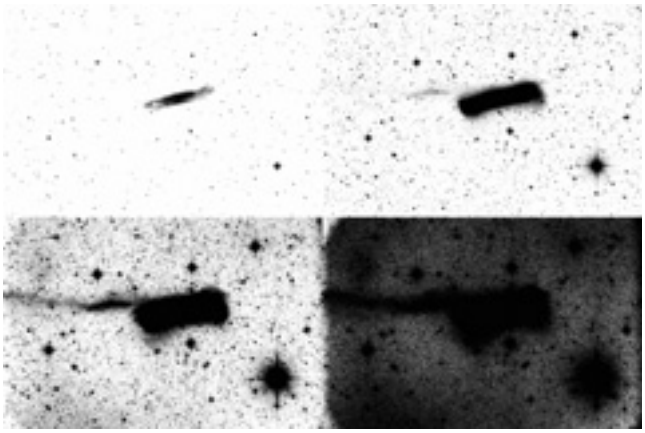

Figure 25. NGC 3628 is displayed from shallow to deep stretch. Notice that the disc grows from roughly normal in appearance to an almost rectangular morphology. This kind of disturbance may give rise to 'rectangular' envelopes seen in some S0 galaxies, like that found in NGC 720. The thickness of the rectangular disc exceeds 50 kpc.

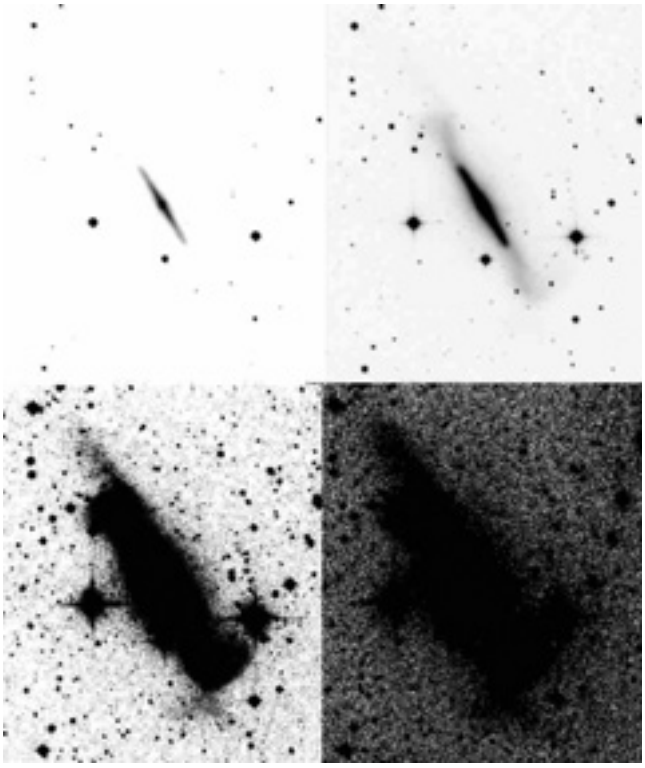

Figure 26. Extreme disturbance of the S0 NGC 4762, displayed with a range of stretch. The shallow exposures follow those in the Hubble Atlas of Galaxies, whilst the deepest stretch shows an almost 'shoe'-like structure resulting from the interaction envelope.

our *HERON* images show an extended 'shoe'-like structure that we suggest may consist of disc stars that were heated or disturbed during an interaction.

We conclude that the outermost detectable envelopes of face-on discs consist of disc stars. This position is based on Fig. 22, our deep imaging of edge-on discs in Figs 24–26, and the edge-on discs in our sample from Fig. A1 (including additional supplemental inverse images). Furthermore, deep H I images (e.g. Sancisi et al. 2008 and

other studies) find H I envelopes around spiral galaxies in the disc plane, including that of M 51. We argue that studies of face-on disc galaxies such as that of Merritt et al. (2016) may in fact be detecting extended disc light. Fig. 23 illustrates our model subtractions of three of the galaxies in Merritt et al. (2016), and in all cases, spiral structure or disturbances dominate the outermost isophotes. Even though Merritt et al. (2016) finds light outside these isophotes, we are not able extend our surface brightness measurements to such a faint level. Even so, we argue that for all disc galaxies, especially those with near face-on inclination, the lines of evidence from our stellar imaging study and that of Sancisi et al. (2008) and similar H I studies, support the outermost visible light isophotes being dominated by stars in the disc plane, not in the spheroidal old halo. These stars may owe their presence to disc flaring. Other evidence arises from studies of the extreme UV (XUV) discs, e.g. Werk et al. (2010). Lemonias et al. (2011) found that 4–14 per cent of galaxies to $z = 0.05$ have XUV discs, with 7–18 per cent of galaxies in the green valley being candidates to transition *away* from the red sequence.

The prima facie evidence of a true Population II halo would be the presence of globular clusters, but detection of globular clusters in sufficient numbers at radii >30 kpc would be difficult even if the spatial resolution were available to resolve them: distant clusters are rare, even in highly populated systems.

6 CONCLUSION

We report new imaging to low surface brightness for a sample of nearby galaxies predominantly from the 2MASS nearby bright galaxy catalogue, and mostly lying within the boundary of the Local Volume ∼50 Mpc. We show that our imaging using the Jeanne Rich C28 0.7-m telescope reaches ∼28 mag arcsec^{-2}, and reproduces well the low surface brightness structures and surface brightness profiles reported in the literature. In ∼1 h exposures, we reproduce published faint structure from amateur exposures of tens of hours, Dragonfly, and the CFHT. We did not fail to measure, or observe, any low surface brightness features reported by others in the literature.

We measure the diameters of the envelopes not including transient structures such as streams, arcs, and interaction filaments. We find a strong primary correlation between envelope diameter and M_V, after carefully checking for spurious correlations between envelope diameter and apparent surface brightness, and distance. We find that the largest envelopes are hosted by the most luminous elliptical galaxies. However, very large envelopes are found spanning the full range of morphological types in the most luminous galaxies.

We consider our sample in the colour–magnitude diagram. Whilst the largest envelopes are found in all parts of the CMD, the envelopes with $D > 100$ kpc are almost always found on the bright end of the red sequence, with $M_V < -21$ in E/S0 galaxies. The largest envelopes, those with $D > 40$ kpc, are only found in galaxies with $M_V < -20$; however, 80 per cent of the envelopes with $D > 60$ kpc are on the bright end of the red sequence. We find that interactions can occur with equal likelihood across the CMD, even on the red sequence. Although we can observe signs of interactions in the last 1–2 Gyr, these are not necessarily playing a role in quenching of star formation as evidenced by the galaxy color-magnitude plot. However, this question deserves more exploration, potentially in a future *HERON* project.

It is noteworthy to emphasize that it is mostly the total intrinsic luminosity, and *not* presence on the red sequence, that determines envelope diameter. Galaxies at the faint ends ($M_V > -21$) of the blue and red sequences have the same distribution of envelope sizes. Whilst presence on the red sequence may have resulted from an early interaction history, the present-day absolute luminosity appears to be the critical factor that determines the size of the low surface brightness envelope.

We consider disc galaxies and find that edge-on spirals have comparable to those of diameters than face-on spirals. We develop several lines of argument that the envelopes of disc galaxies are dominated by stars on the disc plane. We show that in the sample of Merritt et al. (2016) that the outermost portions of discs are dominated by spiral structure. We also illustrate two cases, NGC 4762 and NGC 3628, where interactions have resulted in the disc outskirts being strongly disturbed and thickened. Appealing to the H I imaging of Sancisi et al. (2008) and studies of XUV discs (Lemonias et al. 2011), we argue that the envelopes of discs are dominated by disc stars, not by the classical halo spheroid. The low surface brightness structures of all edge-on galaxies are dominated by their discs; there are no cases where the greatest diameter at low surface brightness arises from a classical spheroidal structure.

Future *HERON* work amongst an international team of observational and theoretical collaborators will report the quantitative analysis of surface brightness profiles, discuss outer envelope morphologies, and other properties including comparisons of extended structures in multiple wavelengths. We will also report and catalogue all low surface brightness companions detected in our survey, listing luminosities, diameters, and coordinates amongst other details. Finally, we will upload our complete data sets and imaging to the *HERON* archive at the IRSA/IPAC data base.

ACKNOWLEDGEMENTS

The authors express thanks to Eija Laurikannen and Sebastien Comeron for valuable comments on the project. We would like to thank UCLA alumnus Kyra Mitchell for her valuable help creating our catalogue of inverse image grids, several of which are displayed in the Appendix with the rest included as supplemental materials (Fig. A1). We acknowledge UCLA alumnus Dylan Schaul, who worked on data reduction for the early images. We also acknowledge Nanjing University (Jiangsu Province, China) students Xu Zizheng and Weigung Cao for their help creating an image reduction pipeline that will be used in our future work. We also thank David Gedalia for his assistance in improvements of the 0.7-m Lockwood Valley telescope, and B. Megdal for his assistance in obtaining images using his 8-inch refractor. We also acknowledge Ian Kearns-Brown for technical and IT support of the Jeanne Rich telescope. We also thank the membership of the Polaris Observatory Association for their maintenance of the observatory infrastructure. Aleksandr Mosenkov expresses gratitude for the grant of the Russian Foundation for Basic Researches number mol_a 18-32-00194. RMR acknowledges financial support from his late father Jay Baum Rich.

This research has made use of the NASA/IPAC Infrared Science Archive (IRSA; http://irsa.ipac.caltech.edu/frontpage/), and the NASA/IPAC Extragalactic Database (NED; https://ned.ipac.caltech.edu/), both of which are operated by the Jet Propulsion Laboratory, California Institute of Technology, under contract with the National Aeronautics and Space Administration. This research has made use of the HyperLEDA data base (http://leda.univ-lyon1.fr/; Makarov et al. 2014).

Software: IRAF, IMSURFIT, ELLIPSE, DS9, PYTHON, VEUSZ GRAPHING, MICROSOFT EXCEL.

REFERENCES

Abraham R., van Dokkum P., 2015, ApJ, 782, L24
Agertz O., Kravtsov A. V., 2016, ApJ, 824, 79
Ahn C. P. et al., 2014, ApJS, 211, 17
Amorisco N. C., 2017, MNRAS, 469, L48
Arp H., Bertola F., 1969, Astrophys. Lett., 4, 23
Atkinson A. M., Abraham R. G., Ferguson A. M. N., 2013, ApJ, 765, 28
Bechtol K. et al., 2015, ApJ, 807, 50
Behroozi P. S., Wechsler R. H., Wu H.-Y., Busha M. T., Klypin A. A., Primack J. R., 2013, ApJ, 763, 18
Bellazzini M., Cacciari C., Federici L., Fusi Pecci F., Rich M., 2003, A&A, 405, 867
Bell E. F., McIntosh D. H., Katz N., Weinberg M. D., 2003, ApJS, 149, 289
Belokurov V. et al., 2006, ApJ, 642, L137
Belokurov V. et al., 2007a, ApJ, 658, 337
Belokurov V. et al., 2007b, ApJ, 654, 897
Bertin E., Arnouts S., 1996, A&AS, 117, 393
Binggeli B., Sandage A., Tammann G. A., 1988, ARA&A, 26, 509
Blauensteiner M., Remmel P., Riepe P., Strauß H., Trulson U., Zilch T., Karachentsev I. D., Sharina M. E., 2017, Astrophysics, 60, 295
Boylan-Kolchin M., Bullock J. S., Kaplinghat M., 2011, MNRAS, 415, L40
Boylan-Kolchin M., Bullock J. S., Kaplinghat M., 2012, MNRAS, 422, 1203
Brosch N., 2015, MNRAS, 454, 3222
Brosch N., Polishook D., Shporer A., Kaspi S., Berwald A., Manulis I., 2008, Ap&SS, 314, 163
Brosch N., Kaspi S., Niv S., Manulis I., 2015, Ap&SS, 359, 9
Brosch N., Koriski S., Rich R. M., Mosenkov A. V., 2019, MNRAS, 482, 2284
Brown T. M., Ferguson H. C., Smith E., Kimble R. A., Sweigart A. V., Renzini A., Rich R. M., VandenBerg D. A., 2003, ApJ, 592, L17
Brown T. M., Smith E., Ferguson H. C., Rich R. M., Guhathakurta P., Renzini A., Sweigart A. V., Kimble R. A., 2006, ApJ, 652, 323
Bullock J. S., Johnston K. V., 2005, ApJ, 635, 931
Bullock J. S., Kravtsov A. V., Weinberg D. H., 2000, ApJ, 539, 517
Bullock J. S., Kravtsov A. V., Weinberg D. H., 2001, ApJ, 548, 33
Bureau M., Freeman K. C., 1999, AJ, 118, 126
Chambers K. C. et al., 2016, preprint (arXiv:1612.05560)
Cole S., Lacey C. G., Baugh C. M., Frenk C. S., 2000, MNRAS, 319, 168
Cooper A. P. et al., 2010, MNRAS, 406, 744
Cooper A. P., D'Souza R., Kauffmann G., Wang J., Boylan-Kolchin M., Guo Q., Frenk C. S., White S. D. M., 2013, MNRAS, 434, 3348
Cunningham E. C. et al., 2016, ApJ, 820, 18
de Vaucouleurs G., 1969, Astrophys. Lett., 4, 17
Di Cintio A., Brook C. B., Macciò A. V., Stinson G. S., Knebe A., Dutton A. A., Wadsley J., 2014, MNRAS, 437, 415
Duc P.-A., Cuillandre J.-C., Renaud F., 2018, MNRAS, 475, L40
Duc P.-A., 2017, IAUS, 321, 180
Duc P.-A. et al., 2015, MNRAS, 446, 120
Durrell P. R., Harris W. E., Pritchet C. J., 2001, AJ, 121, 2557
Elias L. M., Sales L. V., Creasey P., Cooper M. C., Bullock J. S., Rich M. R., Hernquist L., 2018, MNRAS, 479, 4004
Fakhouri O., Ma C.-P., Boylan-Kolchin M., 2010, MNRAS, 406, 2267
Ferguson H. C., Sandage A., 1989, ApJ, 346, L53
Ferrarese L. et al., 2006, ApJS, 164, 334
Finkbeiner D. P. et al., 2016, ApJ, 822, 66
Flewelling H. A. et al., 2016, preprint (arXiv:1612.05243)
Gaia Collaboration et al., 2016, A&A, 595, A1
Gaia Collaboration et al., 2018, A&A, 616, A1
Garrison-Kimmel S. et al., 2017a, MNRAS, 471, 1709
Garrison-Kimmel S., Bullock J. S., Boylan-Kolchin M., Bardwell E., 2017b, MNRAS, 464, 3108
Governato F. et al., 2010, Nature, 463, 203
Green G. M., Schlafly E. F., Zucker C., Speagle J. S., Finkbeiner D. P., 2019, preprint (arXiv:1905.02734)
Harmsen, Monachesi, Bell, de Jong, Bailin, Radburn-Smith, Holwerda, 2017, MNRAS, 466, 1491
Hood C. E., Kannappan S. J., Stark D. V., Dell'Antonio I. P., Mofffett A. J., Eckert K. D., Norris M. A., Hendel D., 2018, ApJ, 857, 144
Ibata R. A. et al., 2013, Nature, 493, 62
Jarrett T. H., Chester T., Cutri R., Schneider S. E., Huchra J. P., 2003, AJ, 125, 525
Javanmardi B. et al., 2016, A&A, 588, A89
Johnston K. V., 1998, ApJ, 495, 297
Karabal E., Duc P.-A., Kuntschner H., Chanial P., Cuillandre J.-C., Gwyn S., 2017, A&A, 601, A86
Karachentsev I. D., 1965, ApJ, 1, 118
Karachentsev I. D., Makarova L. N., Tully R. B., Rizzi L., Karachentseva V. E., Shaya E. J., 2017, MNRAS, 469, L113
Kazantzidis S., Bullock J. S., Zentner A. R., Kravtsov A. V., Moustakas L. A., 2008, ApJ, 688, 254
Klypin A., Kravtsov A. V., Valenzuela O., Prada F., 1999, ApJ, 522, 82
Koch A. et al., 2008, ApJ, 689, 958
Koch A., Burkert A., Rich R. M., Collins M. L. M., Black C. S., Hilker M., Benson A. J., 2012, ApJ, 755, L13
Kormendy J., Bahcall J. N., 1974, AJ, 79, 671
Kormendy J., Fisher D. B., Cornell M. E., Bender R., 2009, ApJS, 182, 216
Lemonias J. J. et al., 2011, ApJ, 733, 74
Lundmark K., 1920, KSVH, 60, 1
Mackey A. D., Koposov S. E., Erkal D., Belokurov V., Da Costa G. S., Gómez F. A., 2016, MNRAS, 459, 239
Makarov D., Prugniel P., Terekhova N., Courtois H., Vauglin I., 2014, A&A, 570, A13
Malin D. F., 1978, Nature, 276, 591
Malin D. F., 1979, Nature, 277, 279
Malin D. F., Carter D., 1980, Nature, 285, 643
Malin D., Hadley B., 1997, ASPC, 116, 460
Martínez-Delgado D. et al., 2010, AJ, 140, 962
Martínez-Delgado D. et al., 2012, ApJ, 748, L24
McConnachie A. W. et al., 2009, Nature, 461, 66
Merritt A., van Dokkum P., Abraham R., Zhang J., 2016, ApJ, 830, 62
Mihos J. C., Harding P., Feldmeier J., Morrison H., 2005, ApJ, 631, L41
Mihos J. C., Harding P., Feldmeier J. J., Rudick C., Janowiecki S., Morrison H., Slater C., Watkins A., 2017, ApJ, 834, 16
Miskolczi A., Bomans D. J., Dettmar R.-J., 2011, A&A, 536, A66
Monachesi A., Bell E. F., Radburn-Smith D. J., Bailin J., de Jong R. S., Holwerda B., Streich D., Silverstein G., 2016, MNRAS, 457, 1419
Moore B., Ghigna S., Governato F., Lake G., Quinn T., Stadel J., Tozzi P., 1999, ApJ, 524, L19
Morales G., Martínez-Delgado D., Grebel E. K., Cooper A. P., Javanmardi B., Miskolczi A., 2018, A&A, 614, A143
Mori M., Rich R. M., 2008, ApJ, 674, L77
Mouhcine M., Ferguson H. C., Rich R. M., Brown T. M., Smith T. E., 2005, ApJ, 633, 821
Müller O. et al., 2019, A&A, 624, L6
Muñoz-Mateos J. C. et al., 2015, ApJS, 219, 3
Muslimov E. et al., 2017, Appl. Opt., 56, 8639
Paudel S., Ree C. H., 2014, ApJ, 796, L14
Pease F. G., 1920, ApJ, 51, 276
Peng C. Y., Ho L. C., Impey C. D., Rix H.-W., 2002, AJ, 124, 266
Peng C. Y., Ho L. C., Impey C. D., Rix H.-W., 2010, AJ, 139, 2097
Pillepich A., Madau P., Mayer L., 2015, ApJ, 799, 184
Purcell C. W., Bullock J. S., Kazantzidis S., 2010, MNRAS, 404, 1711
Read J. I., Iorio G., Agertz O., Fraternali F., 2017, MNRAS, 467, 2019
Rich R. M., Mighell K. J., Freedman W. L., Neill J. D., 1996, AJ, 111, 768
Rich R. M., Collins M. L. M., Black C. M., Longstaff F. A., Koch A., Benson A., Reitzel D. B., 2012, Nature, 482, 192
Rich R. M. et al., 2017, IAUS, 321, 186
Sancisi R., Fraternali F., Oosterloo T., van der Hulst T., 2008, A&AR, 15, 189
Sandin C., 2014, A&A, 567, A97
Sandin C., 2015, A&A, 577, A106
Schlafly E. F., Finkbeiner D. P., 2011, ApJ, 737, 103

Sérsic J. L., 1968, Atlas de Galaxias Australes. Argentina Observatorio Astronomico, Cordoba
Shi D. D. et al., 2017, ApJ, 846, 26
Stewart K. R., Bullock J. S., Wechsler R. H., Maller A. H., Zentner A. R., 2008, ApJ, 683, 597
Tal T., van Dokkum P. G., Nelan J., Bezanson R., 2009, AJ, 138, 1417
Trujillo I., Fliri J., 2016, ApJ, 823, 123
van Dokkum P. G., Abraham R., Merritt A., 2014, ApJ, 782, L24
van Dokkum P. G., Abraham R., Merritt A., Zhang J., Geha M., Conroy C., 2015, ApJ, 798, L45
Watkins A. E., Mihos J. C., Harding P., 2015, ApJ, 800, L3
Werk J. K. et al., 2010, AJ, 139, 279
Wetzel A. R., Hopkins P. F., Kim J.-. hoon ., Faucher-Giguère C.-A., Kereš D., Quataert E., 2016, ApJ, 827, L23
White D. J., Daw E. J., Dhillon V. S., 2011, Class. Quantum Gravity, 28, 085016
Zwicky F., 1956, ErNW, 29, 344

APPENDIX A: *HERON* IMAGES

See Fig. A1.

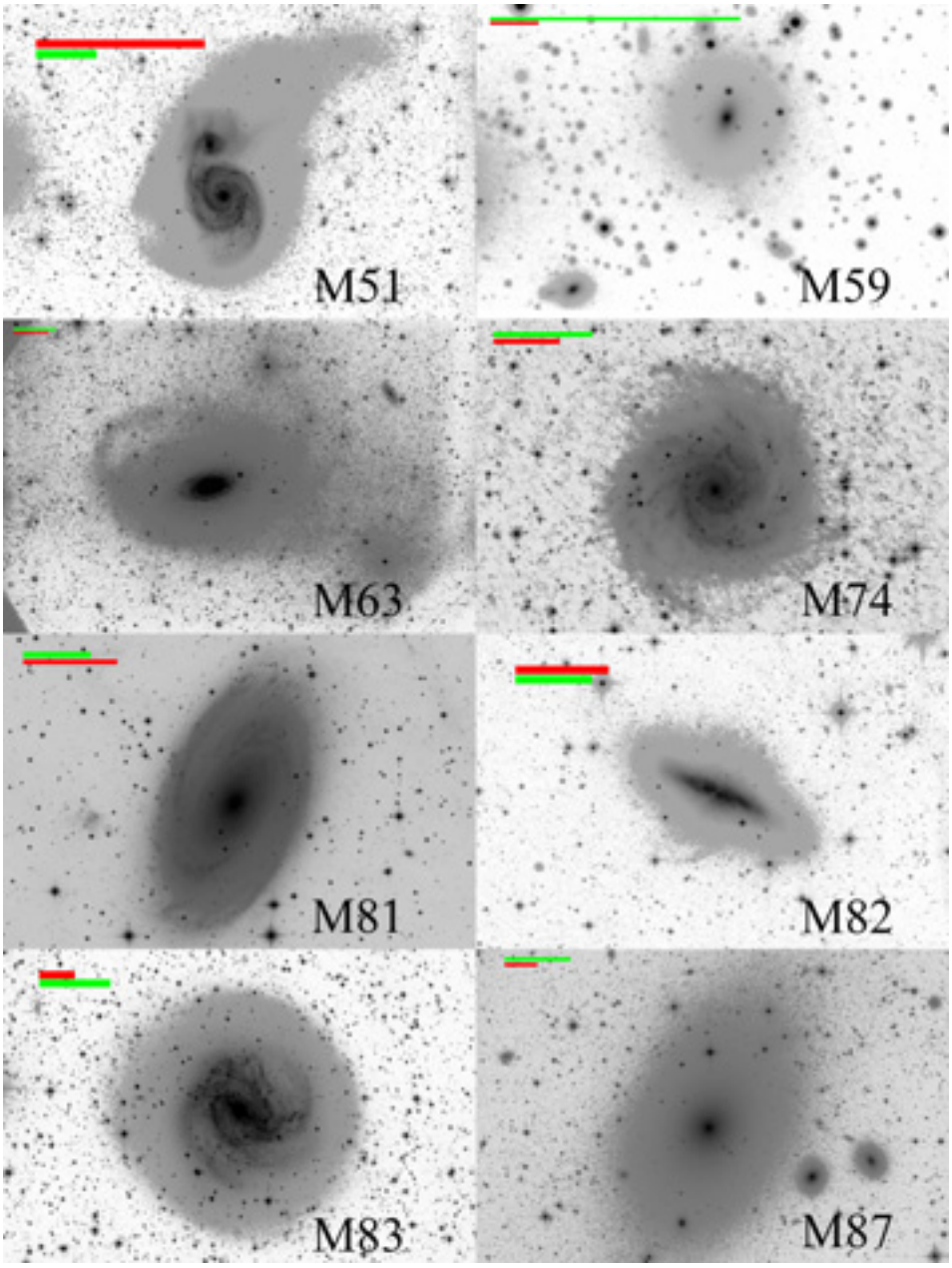

Figure A1. Inverse images of some galaxies from our sample North up; East to the left. The green scale bar is 5 arcmin; the red scale bar is 10 kpc at the distance of the galaxy as listed in Table B1.

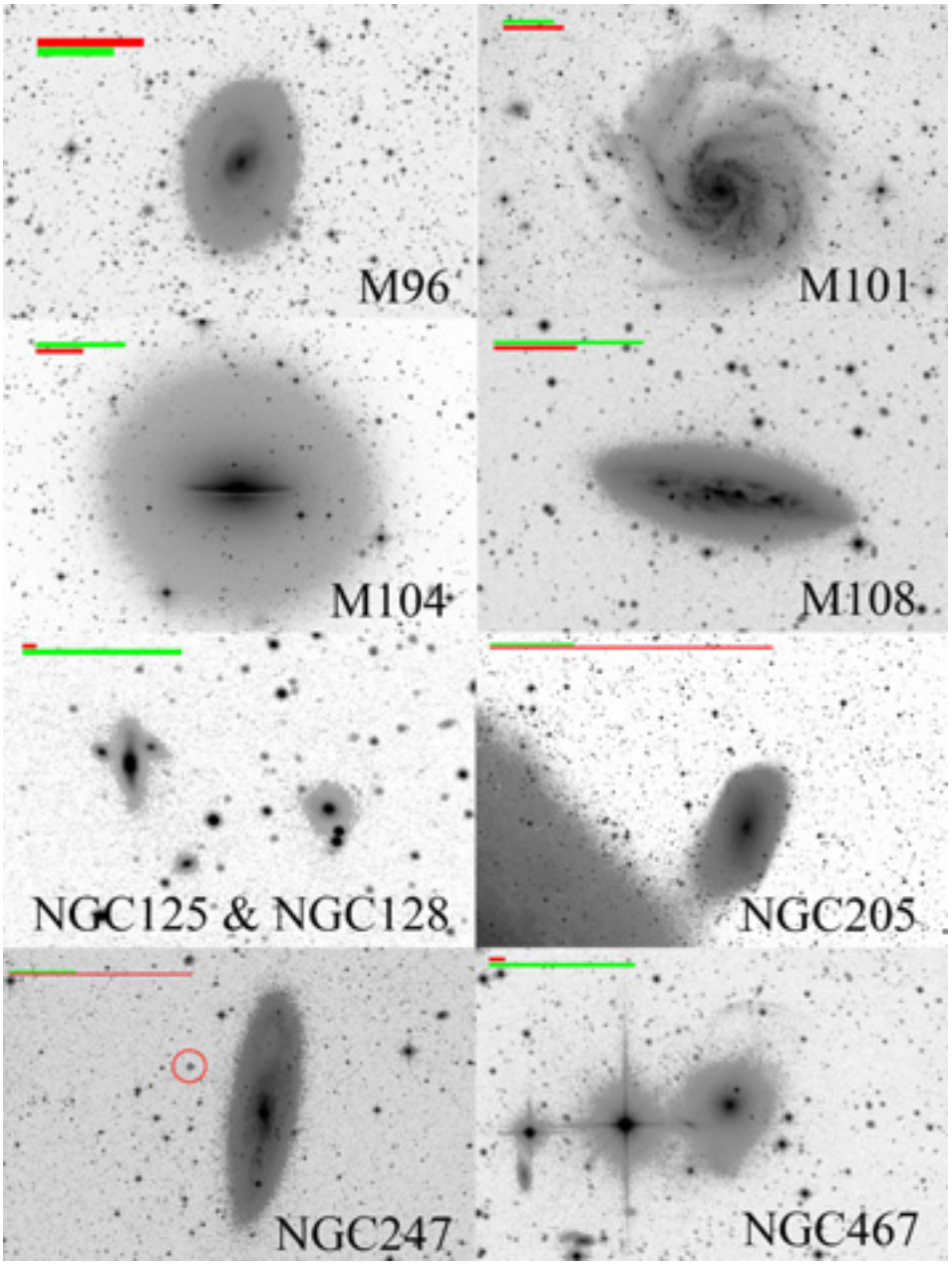

Figure A1. (continued)

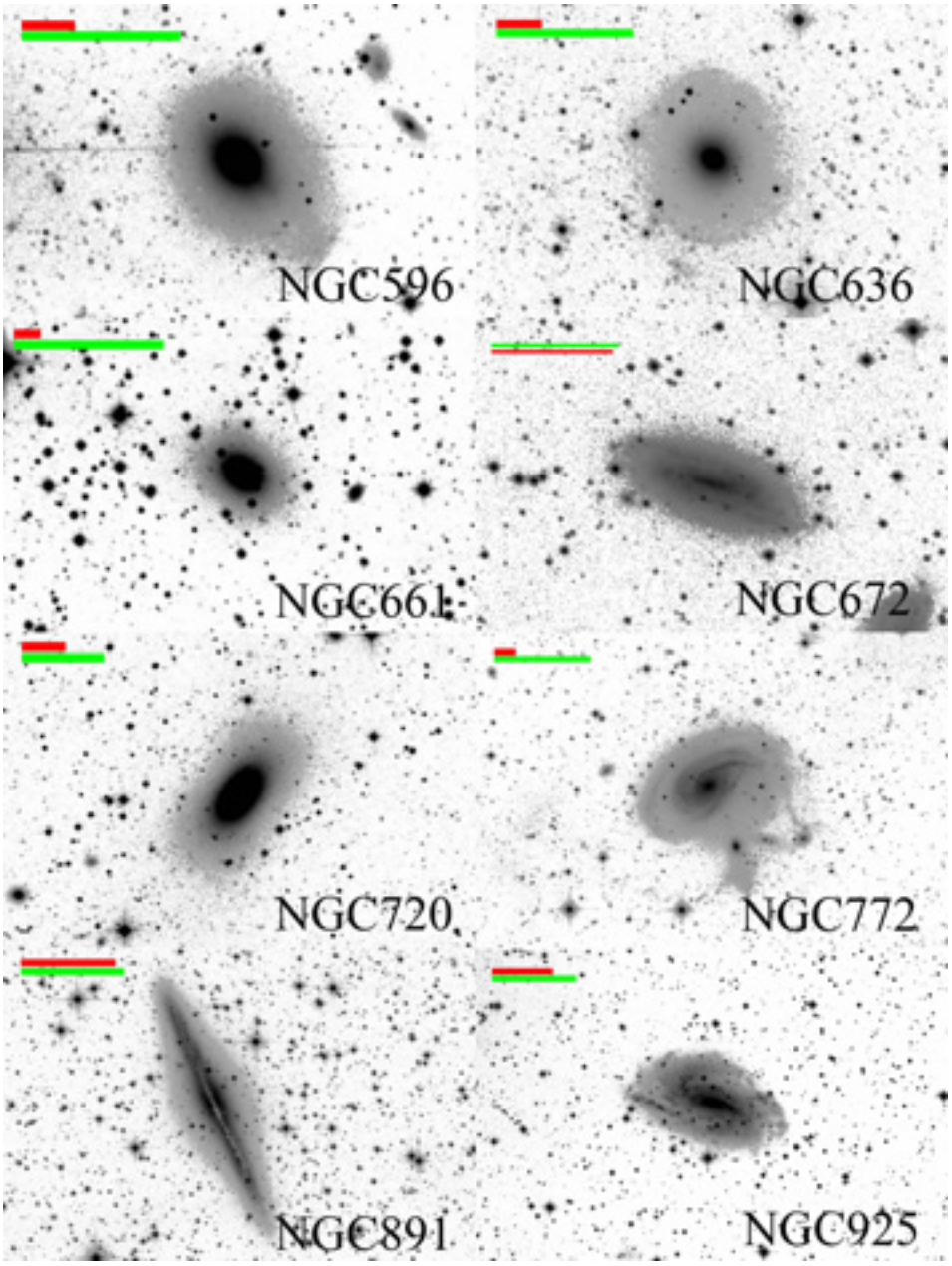

Figure A1. (continued)

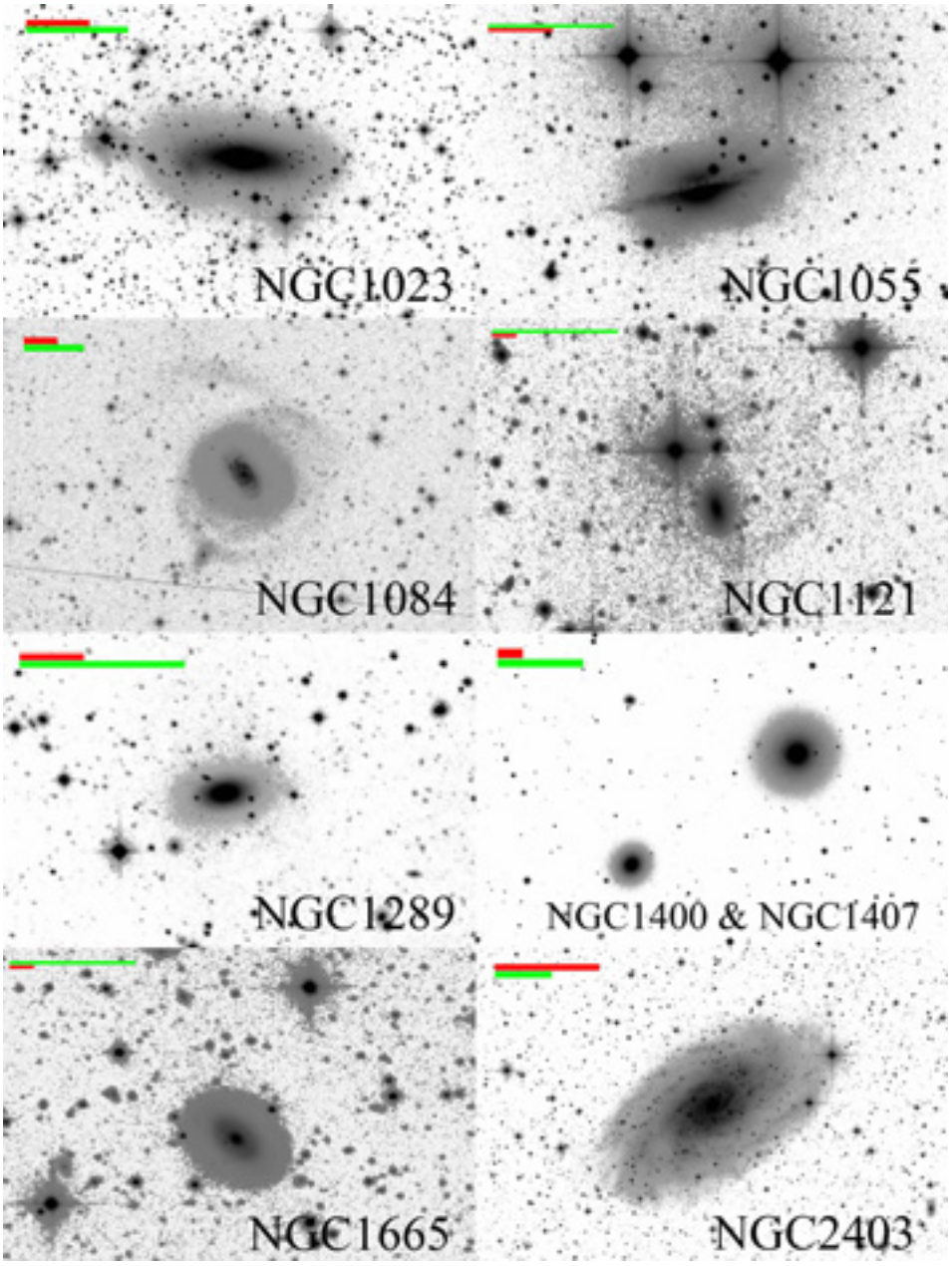

Figure A1. (continued)

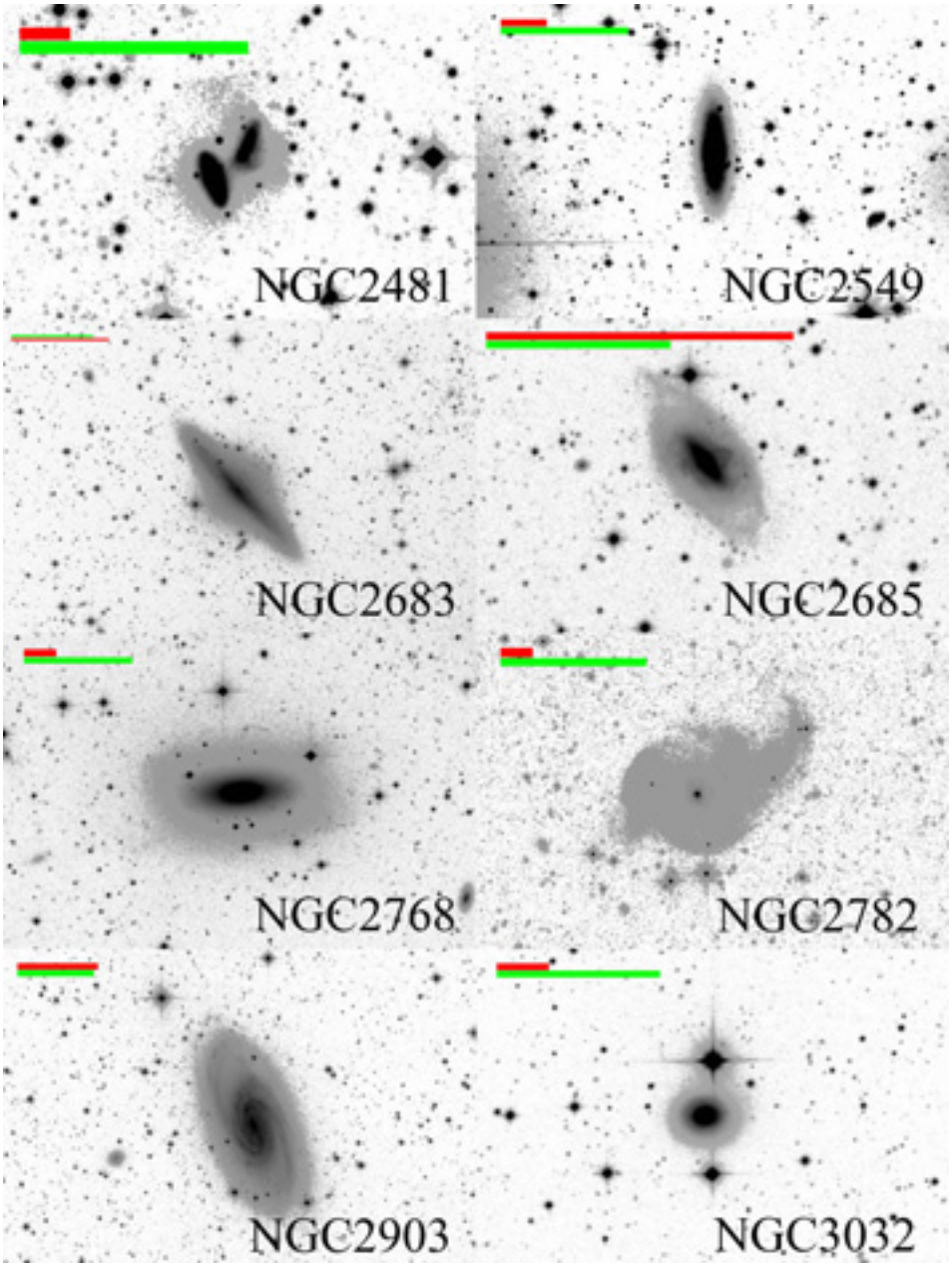

Figure A1. (continued; NGC3077-7743 are published electronically)

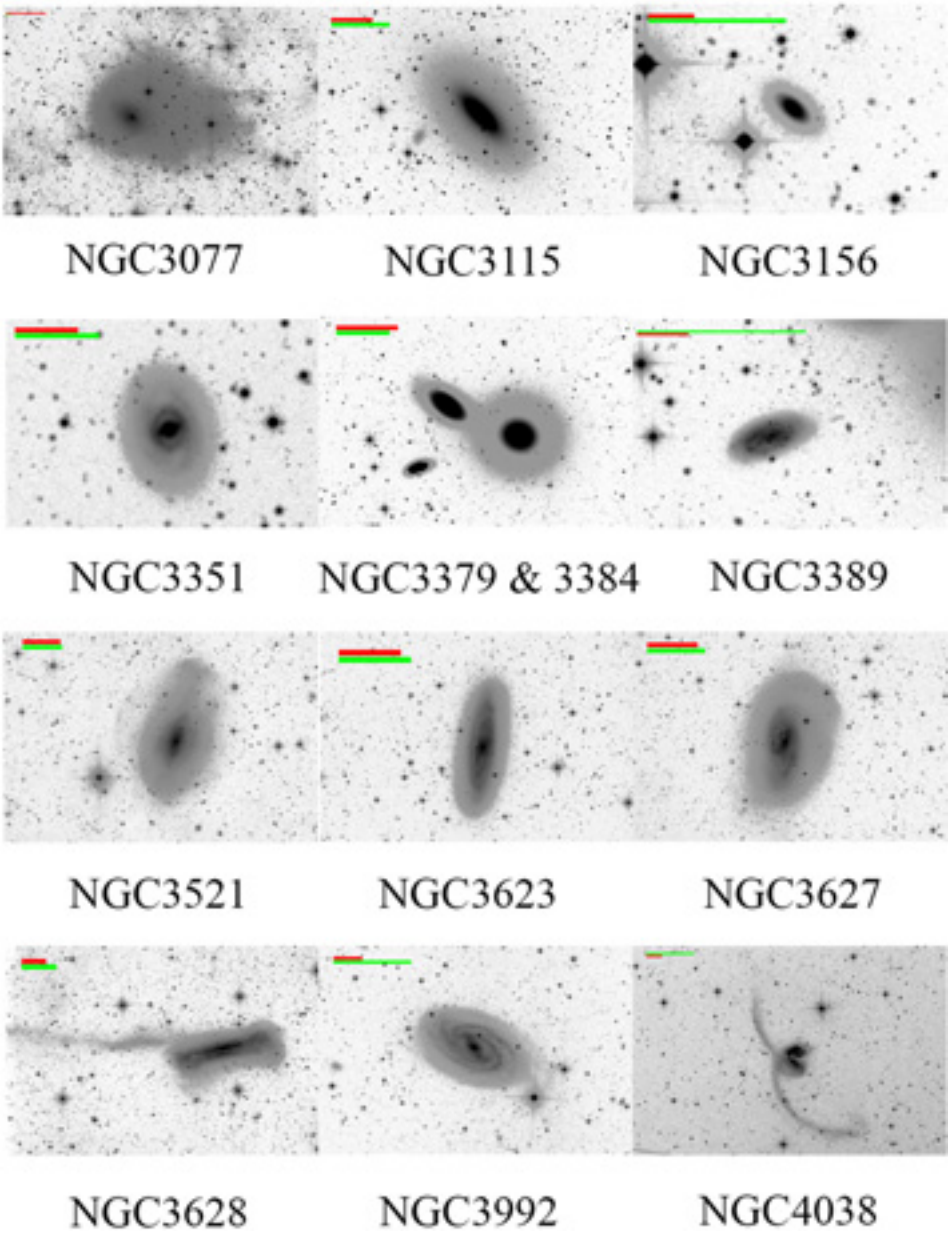

Figure A1. (continued)

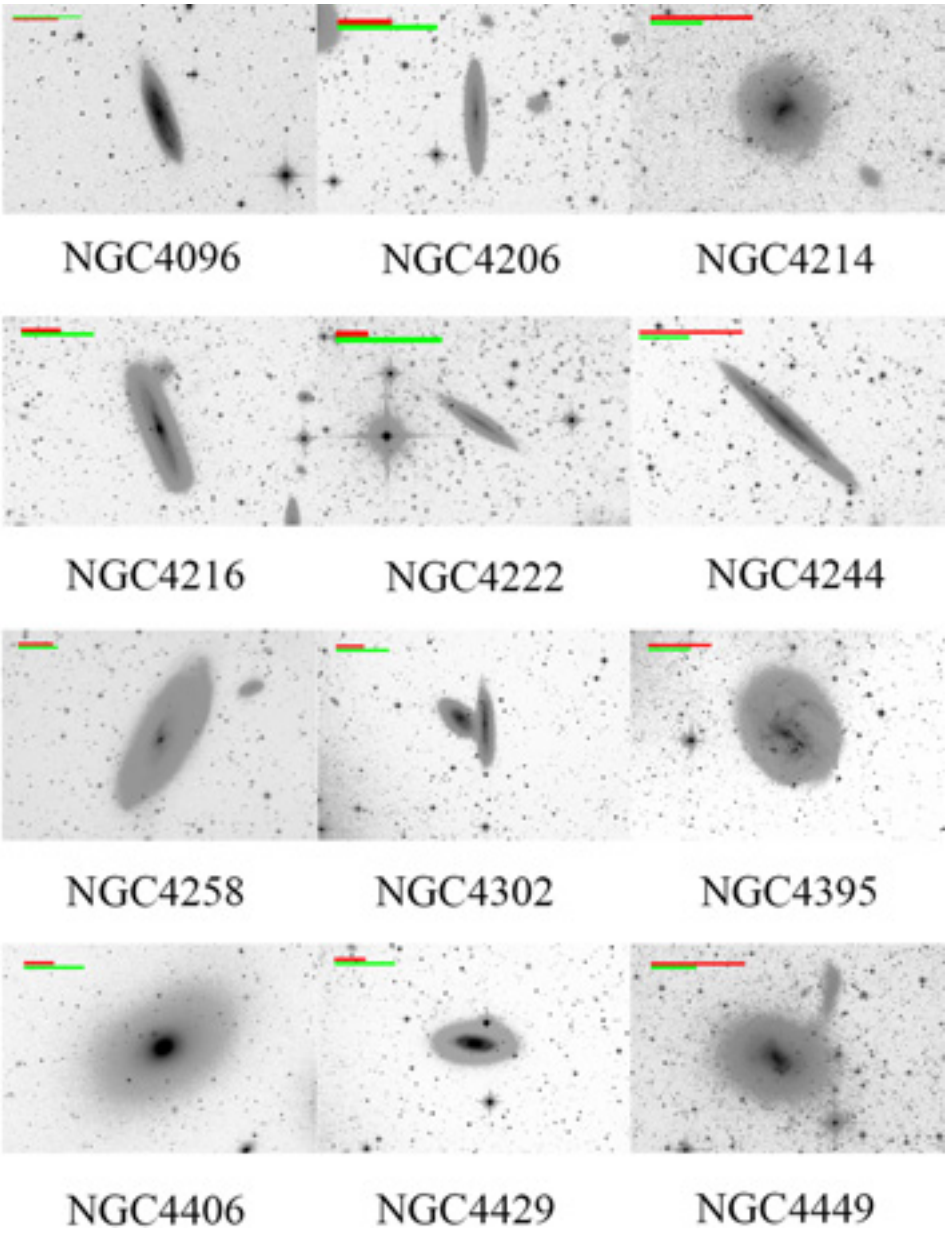

Figure A1. (continued)

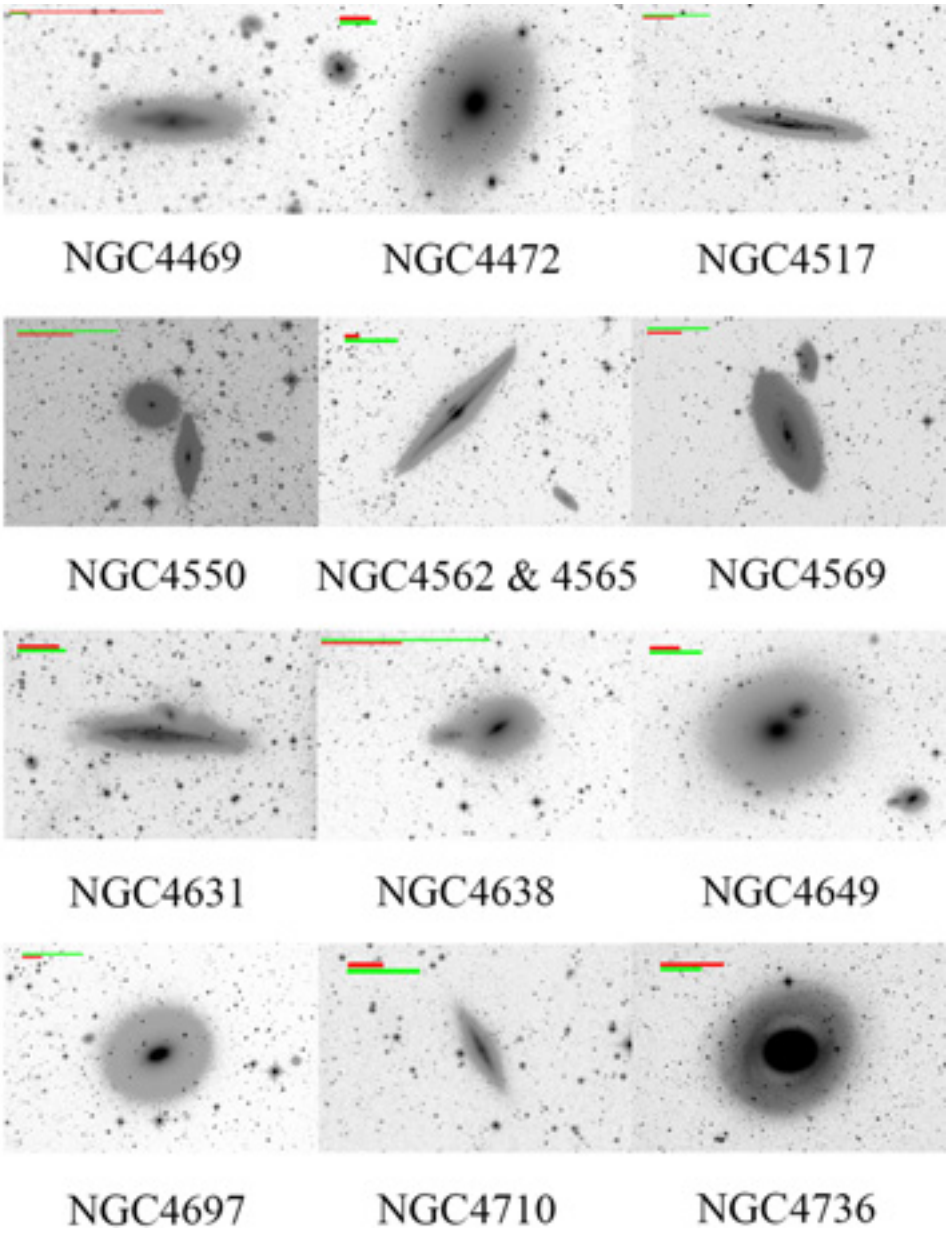

Figure A1. (continued)

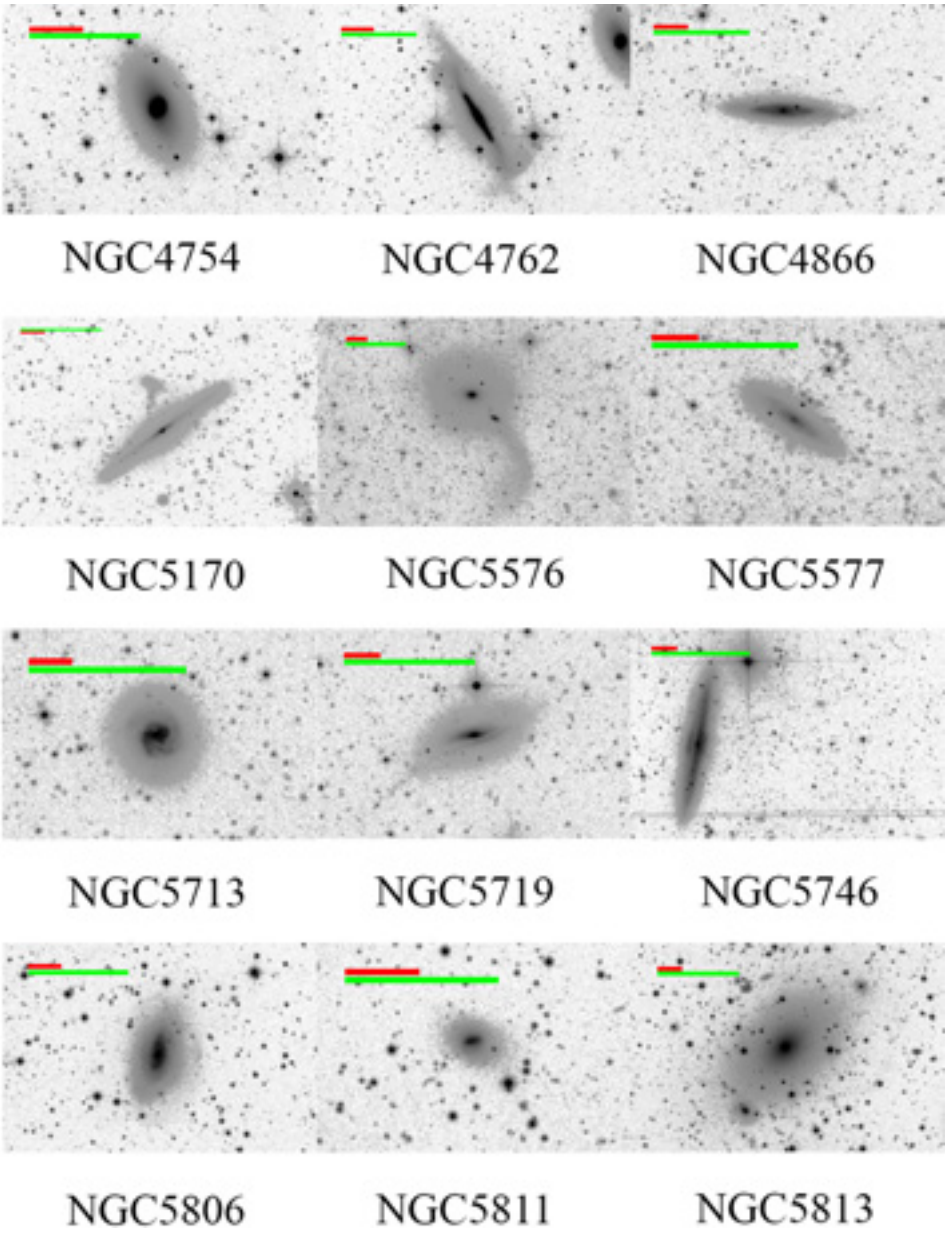

Figure A1. (continued)

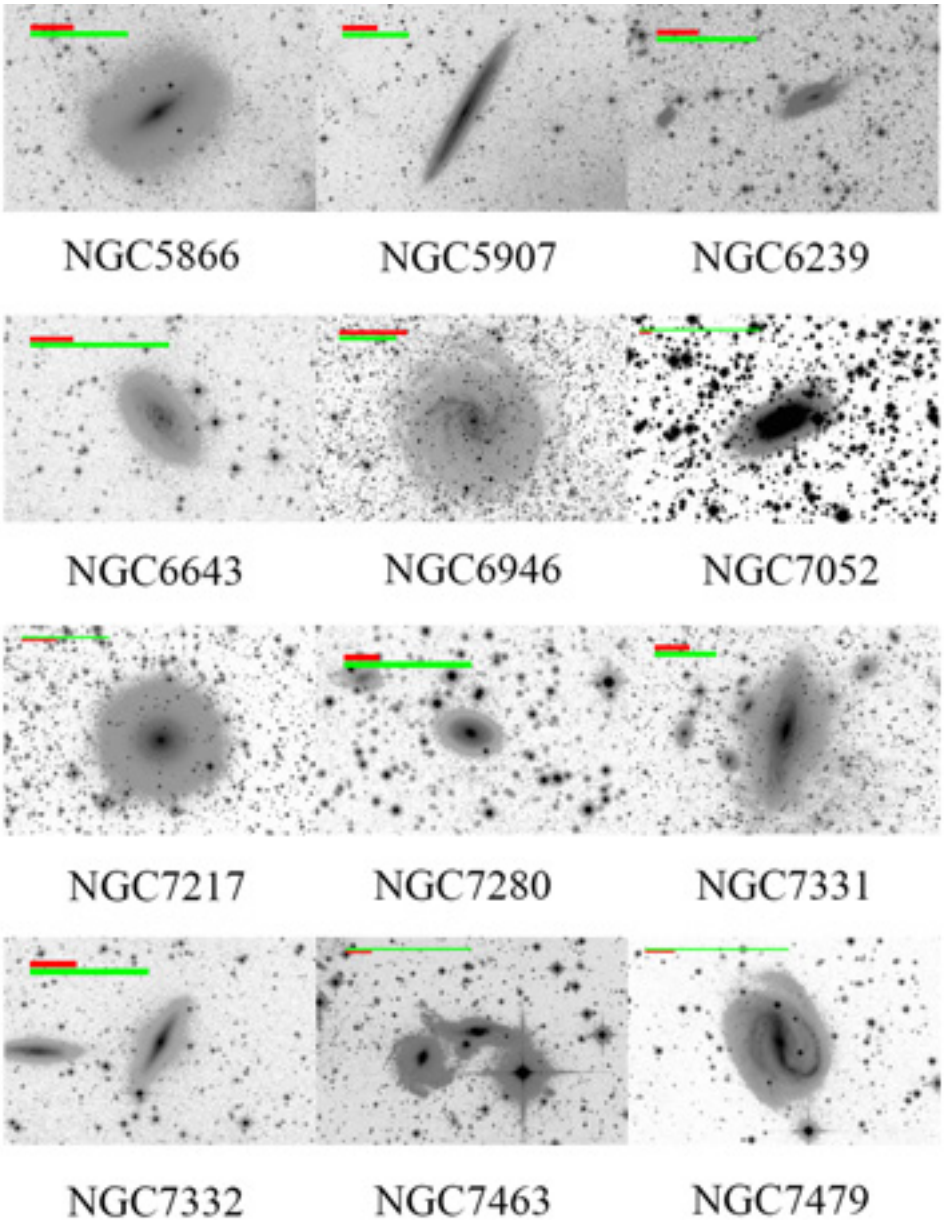

Figure A1. (continued)

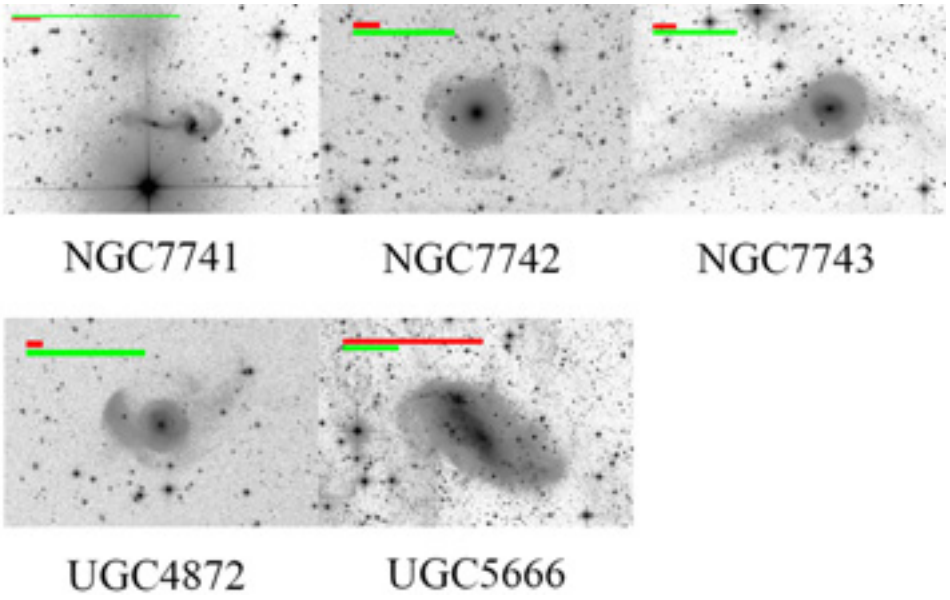

Figure A1. (continued)

APPENDIX B: *HERON* TABLES

See Tables B1–B3.

Table B1. Lists the coordinates (from HyperLeda), distance (see the text), radial velocity (from HyperLeda), type (from NED), apparent and absolute magnitude in the *V* band and the colour $B-V$ (using the HyperLeda values *btc* and *bvtc*). Also, in the column Features we note if a galaxy is viewed edge-on ('E') or interacting ('I').

NGC	RA, Dec. (J2000) (h, deg)	D (Mpc)	v (km s^{-1})	Type	Features	m_V (mag)	M_V (mag)	$B-V$ (mag)
M49(4472)	$12^h29^m46^s$ $+07^h59^m59^s$	16.63	978	E2/S0	–	8.32	−22.79	0.93
M51(5194/5195)	$13^h29^m52^s$ $+47^h11^m42^s$	8.58	460	SA(s)bc	I	7.81	−21.86	0.55
M59(4621)	$12^h42^m02^s$ $+11^h38^m50^s$	14.74	438	E5	–	9.54	−21.31	0.91
M60(4649)	$12^h43^m39^s$ $+11^h33^m09^s$	17.05	1107	E2	I	8.74	−22.41	0.94
M63(5055)	$13^h15^m49^s$ $+42^h01^m45^s$	9.04	507	SA(rs)bc	–	8.24	−21.54	0.66
M65(3623)	$11^h18^m55^s$ $+13^h05^m32^s$	12.87	801	SAB(rs)a	–	8.81	−21.74	0.78
M66(3627)	$11^h20^m15^s$ $+12^h59^m29^s$	11.46	718	SAB(s)b	–	8.47	−21.82	0.63
M74(628)	$01^h36^m41^s$ $+15^h47^m00^s$	10.14	658	SA(s)c	–	8.91	−21.12	0.49
M81(3031)	$09^h55^m33^s$ $+69^h03^m54^s$	3.60	−37	SA(s)ab	–	6.29	−21.49	0.83
M82(3034)	$09^h55^m52^s$ $+69^h40^m47^s$	3.62	231	I0	E	7.07	−20.72	0.69
M83(5236)	$13^h37^m00^s$ $-29^h51^m56^s$	4.90	508	SAB(s)c	–	6.95	−21.50	0.60
M86(4406)	$12^h26^m11^s$ $+12^h56^m44^s$	17.39	−291	S0(3)/E3	–	8.72	−22.48	0.91
M87(4486)	$12^h30^m49^s$ $+12^h23$m25^s	16.78	1283	E+	–	8.62	−22.50	0.93
M90(4569)	$12^h36^m49^s$ $+13^h09^m48^s$	11.86	−220	SAB(rs)ab	–	8.91	−21.46	0.61
M94(4736)	$12^h50^m53^s$ $+41^h07^m13^s$	4.39	313	(R)SA(r)ab	–	7.83	−20.38	0.72
M95(3351)	$10^h43^m57^s$ $+11^h42^m13^s$	9.93	777	SB(r)b	–	9.43	−20.55	0.73
M96(3368)	$10^h46^m45^s$ $+11^h49^m11^s$	9.79	892	SAB(rs)ab	–	8.96	−21.00	0.80
M101(5457)	$14^h03^m12^s$ $+54^h20^m56^s$	7.11	236	SAB(rs)cd	–	7.86	−21.40	0.44
M104(4594)	$12^h39^m59^s$ -11^h37m22^s	8.60	1087	SA(s)a	E	7.85	−21.82	0.88
M105(3379)	10^h47m49^s $+12^h34$m53^s	11.32	918	E1	I	9.19	−21.08	0.93
M106(4258)	$12^h18^m57^s$ $+47^h18^m13^s$	7.61	454	SAB(s)bc	–	7.88	−21.53	0.60
M108(3556)	$11^h11^m30^s$ $+55^h40^m27^s$	9.83	697	SB(s)cd	E	9.41	−20.56	0.57
M109(3992)	$11^h57^m35^s$ $+53^h22^m28^s$	25.27	1047	SB(rs)bc	–	9.40	−22.61	0.71
M110(205)	$00^h40^m22^s$ $+41^h41^m07^s$	0.80	−241	E5	–	7.87	−16.65	0.80
125	$00^h28^m50^s$ $+02^h50^m20^s$	63.68	5273	(R)SA0+	–	12.24	−21.78	0.89
128	$00^h29^m15^s$ $+02^h51^m50^s$	44.87	4129	S0	EI	11.58	−21.68	0.90
247	$00^h47^m08^s$ $-20^h45^m37^s$	3.71	155	SAB(s)d	–	8.18	−19.67	0.44
278	$00^h52^m04^s$ $+47^h33^m01^s$	17.78	639	SAB(rs)b	–	10.44	−20.81	0.51

Table B1 – *continued*

NGC	RA, Dec. (J2000) (h, deg)	D (Mpc)	v (km s^{-1})	Type	Features	m_V (mag)	M_V (mag)	$B-V$ (mag)
467	$01^h19^m10^s$ $+03^h18^m02^s$	58.61	5568	SA(s)0	I	11.98	−21.86	0.96
470	$01^h19^m44^s$ $+03^h24^m35^s$	48.75	2373	SA(rs)b	I	11.38	−22.06	0.66
474	$01^h20^m06^s$ $+03^h24^m55^s$	27.54	2342	(R')SA(s)0	I	11.42	−20.78	0.81
509	$01^h23^m24^s$ $+09^h26^m00^s$	32.89	2273	S0	–	13.67	−18.91	0.74
518	$01^h24^m17^s$ $+09^h19^m51^s$	38.73	2685	Sa	E	12.89	−20.05	0.74
520	$01^h24^m35^s$ $+03^h47^m32^s$	17.86	2161	Sa	I	10.99	−20.27	0.70
524	$01^h24^m7^s$ $+09^h32^m19^s$	32.58	2422	SA(rs)0+	–	10.11	−22.45	0.96
525	$01^h24^m52^s$ $+09^h42^m11^s$	23.58	1624	S0	–	13.44	−18.42	0.75
530	$01^h24^m41^s$ $-01^h35^m13^s$	71.81	5024	SB0+	E	12.61	−21.68	0.91
532	$01^h25^m17^s$ $+09^h15^m50^s$	34.66	2369	SAb	E	12.30	−20.40	0.86
596	$01^h32^m51^s$ $-07^h01^m53^s$	21.55	1903	E+	–	10.83	−20.83	0.85
636	$01^h39^m06^s$ $-07^h30^m45^s$	29.47	1854	E3	–	11.32	−21.03	0.91
661	$01^h44^m14^s$ $+28^h42^m21^s$	37.15	3817	E+	–	11.99	−20.86	0.88
672	$01^h47^m53^s$ $+27^h25^m55^s$	7.21	426	SB(s)cd	–	9.97	−19.32	0.43
720	$01^h53^m00^s$ $-13^h44^m18^s$	27.38	1717	E5	–	10.10	−22.08	0.95
772	$01^h59^m19^s$ $+19^h00^m27^s$	25.47	2460	SA(s)b	I	9.39	−22.64	0.65
891	$02^h22^m33^s$ $+42^h20^m51^s$	9.85	527	SA(s)b	E	9.04	−20.93	0.71
925	$02^h27^m16^s$ $+33^h34^m44^s$	9.20	553	SAB(s)d	–	9.38	−20.44	0.45
1023	$02^h40^m23^s$ $+39^h03^m47^s$	9.56	645	SB(rs)0−	I	8.42	−21.49	0.92
1055	$02^h41^m45^s$ $+00^h26^m36^s$	19.34	993	SBb	E	10.14	−21.30	0.72
1084	$02^h45^m59^s$ $-07^h34^m42^s$	15.46	1422	SA(s)c	I	10.26	−20.69	0.51
1289	$03^h18^m49^s$ $-01^h58^m23^s$	29.92	2835	SB(rs)0	–	12.34	−20.04	0.80
1400	$03^h39^m30^s$ $-18^h41^m17^s$	26.06	589	SA0−	–	10.79	−21.29	0.90
1407	$03^h40^m11^s$ $-18^h34^m49^s$	28.54	1791	E0	–	9.46	−22.82	0.95
2403	$07^h36^m51^s$ $+65^h36^m08^s$	3.20	140	SAB(s)cd	–	7.78	−19.75	0.38
2481	$07^h57^m13^s$ $+23^h46^m03^s$	31.72	2180	S0/a	I	12.32	−20.19	0.67
2549	$08^h18^m58^s$ $+57^h48^m11^s$	12.51	1075	SA(r)0	E	11.01	−19.48	0.85
2683	$08^h52^m41^s$ $+33^h25^m20^s$	9.38	420	SA(rs)b	E	8.37	−21.50	0.76
2685	$08^h55^m34^s$ $+58^h44^m03^s$	12.65	877	(R)SB0+	I	11.16	−19.35	0.76
2768	$09^h11^m37^s$ $+60^h02^m14^s$	22.15	1397	S0	–	9.71	−22.01	0.92
2782	$09^h14^m05^s$ $+40^h06^m49^s$	16.98	2623	SAB(rs)a	I	11.50	−19.65	0.61
2903	$09^h32^m10^s$ $+21^h30^m05^s$	9.32	555	SAB(rs)bc	–	8.28	−21.57	0.57
3032	$09^h52^m08^s$ $+29^h14^m11^s$	20.00	1540	SAB(r)0	–	12.34	−19.16	0.64
3079	$10^h01^m58^s$ $+55^h40^m47^s$	16.52	1163	SB(s)c	E	9.45	−21.64	0.53
3115	$10^h05^m13^s$ $-07^h43^m06^s$	9.65	648	S0−	E	9.00	−20.92	0.90
3156	$10^h12^m41^s$ $+03^h07^m45^s$	22.15	1346	S0	–	12.21	−19.51	0.71
3384	$10^h48^m16^s$ $+12^h37^m45^s$	9.42	563	SB(s)0−	I	9.90	−19.97	0.88
3389	$10^h48^m27^s$ $+12h31^m59^s$	19.32	1301	SA(s)c	–	11.42	−20.01	0.36
3521	$11^h05^m48^s$ $+00^h02^m05^s$	12.39	801	SAB(rs)bc	–	8.55	−21.92	0.71
3628	$11^h20^m16^s$ $+13^h35^m22^s$	10.82	845	SAb	E	8.49	−21.68	0.68
4038	$12^h01^m53^s$ $-18^h52^m05^s$	24.49	1634	SB(s)m	I	9.82	−22.12	0.57
4096	$12^h06^m01^s$ $+47^h28^m42^s$	11.99	563	SAB(rs)c	–	9.53	−20.87	0.50
4206	$12^h15^m16^s$ $+13^h01^m26^s$	18.87	702	SA(s)bc	E	11.16	−20.22	0.50
4214	$12^h15^m39^s$ $+36^h19^m35^s$	2.98	292	IAB(s)m	–	9.51	−17.86	0.41
4216	$12^h15^m54^s$ $+13^h08^m57^s$	13.80	134	SAB(s)b	E	9.09	−21.61	0.84
4222	$12^h16^m22^s$ $+13^h18^m26^s$	19.73	229	Sc	E	11.57	−19.90	0.67
4244	$12^h17^m29^s$ $+37^h48^m28^s$	4.35	245	SA(s)cd	E	9.33	−18.86	0.41
4302	$12^h21^m42^s$ $+14^h35^m54^s$	14.32	1129	Sc	EI	10.06	−20.72	0.74
4395	$12^h25^m48^s$ $+33^h32^m48^s$	4.76	317	SA(s)m	–	9.55	−18.84	0.34
4429	$12^h27^m26^s$ $+11^h06^m27^s$	13.00	992	SA(r)0+	–	9.85	−20.72	0.89
4449	$12^h28^m11^s$ $+44^h05^m37^s$	4.27	203	IBm	–	8.66	−19.49	0.33
4469	$12^h29^m28^s$ $+08^h45^m00^s$	16.75	582	SB(s)0/a	E	10.85	−20.27	0.86
4517	$12^h32^m45^s$ $+00^h06^m52^s$	8.39	1127	SA(s)cd	E	9.20	−20.42	0.53
4550	$12^h35^m30^s$ $+12^h13^m15^s$	15.28	410	SB0	EI	11.52	−19.40	0.78
4551	$12^h35^m37^s$ $+12^h15^m50^s$	16.06	1200	E2	I	11.79	−19.24	0.90
4565	$12^h36^m20^s$ $+25^h59^m15^s$	12.07	1226	SA(s)b	E	8.30	−22.11	0.68
4631	$12^h42^m07^s$ $+32^h32^m33^s$	7.35	615	SB(s)d	EI	7.61	−21.72	0.39
4638	$12^h42^m47^s$ $+11^h26^m32^s$	17.21	1163	S0−	EI	11.06	−20.12	0.89
4697	$12^h48^m35^s$ $-05^h48^m02^s$	12.23	1240	E6	–	9.25	−21.19	0.87
4710	$12^h49^m38^s$ $+15^h09^m53^s$	16.83	1103	SA(r)0+	E	10.71	−20.42	0.77
4754	$12^h52^m17^s$ $+11^h18^m50^s$	16.02	1317	SB(r)0−	–	10.41	−20.61	0.86
4762	$12^h52^m55^s$ $+11^h13^m51^s$	10.81	973	SB(r)0	E	10.14	−20.03	0.79
4866	$12^h59^m27^s$ $+14^h10^m15^s$	29.65	1984	SB(rs)bc	E	10.93	−21.43	0.74

Table B1 – *continued*

NGC	RA, Dec. (J2000) (h, deg)	D (Mpc)	v (km s^{-1})	Type	Features	m_V (mag)	M_V (mag)	$B-V$ (mag)
5170	$13^h29^m48^s$ $-17^h57^m59^s$	29.30	1502	SA(s)c	E	9.85	−22.48	0.72
5576	$14^h21^m03^s$ $+03^h16^m15^s$	25.20	1422	E3	I	10.80	−21.20	0.85
5577	$14^h21^m13^s$ $+03^h26^m09^s$	19.23	1489	SA(rs)bc	–	11.66	−19.76	0.75
5713	$14^h40^m11^s$ $+00^h17^m20^s$	20.32	1948	SAB(rs)bc	–	10.64	−20.90	0.56
5719	$14^h40^m56^s$ $+00^h19^m05^s$	26.47	1726	SAB(s)ab	–	11.78	−20.32	0.95
5746	$14^h44^m55^s$ $+01^h57^m17^s$	27.04	1711	SAB(rs)b	E	9.38	−22.78	0.77
5806	$15^h00^m00^s$ $+01^h53^m28^s$	20.69	1348	SAB(s)b	–	11.16	−20.42	0.60
5811	$15^h00^m27^s$ $+01^h37^m24^s$	24.17	1523	SB(s)m	–	13.58	−18.34	0.74
5813	$15^h01^m11^s$ $+01^h42^m07^s$	31.87	1955	E1-2	–	10.36	−22.16	0.92
5814	$15^h01^m21^s$ $+01^h38^m13^s$	156.31	10526	(R')Sab	–	13.21	−22.77	0.79
5866	$15^h06^m29^s$ $+55^h45^m47^s$	14.42	674	S0_3	E	9.89	−20.90	0.79
5907	$15^h15^m53^s$ $+56^h19^m44^s$	17.23	667	SA(s)c	E	9.10	−22.08	0.62
6239	$16^h50^m04^s$ $+42^h44^m23^s$	24.30	926	SB(s)b	I	11.91	−20.01	0.41
6340	$17^h10^m24^s$ $+72^h18^m15^s$	19.41	1215	SA(s)0/a	–	10.95	−20.49	0.80
6643	$18^h19^m46^s$ $+74^h34^m06^s$	20.25	1484	SA(rs)c	–	10.48	−21.05	0.52
6946	$20^h34^m52^s$ $+60^h09^m12^s$	6.72	45	SAB(rs)cd	–	8.02	−21.12	0.45
7052	$21^h18^m33^s$ $+26^h26^m47^s$	51.29	4700	E	–	11.72	−21.83	1.71
7217	$22^h07^m52^s$ $+31^h21^m33s$	18.28	951	(R)SA(r)ab	–	9.80	−21.51	0.80
7280	$22^h26^m27^s$ $+16^h08^m53s$	21.48	1862	SAB(r)0+	–	12.03	−19.64	0.83
7331	$22^h37^m04^s$ $+34^h24^m56^s$	14.53	815	SA(s)b	–	8.53	−22.28	0.71
7332	$22^h37^m24^s$ $+23^h47^m53^s$	22.77	1180	S0	E	11.00	−20.78	0.81
7463	$23^h01^m52^s$ $+15^h58^m54^s$	22.82	2262	SABb	I	12.33	−19.46	0.39
7465	$23^h02^m00^s$ $+15^h57^m53^s$	27.29	1948	(R')SB(s)0	I	12.40	−19.78	0.64
7479	$23^h04^m56^s$ $+12^h19^m22^s$	30.20	2380	SB(s)c	–	10.48	−21.92	0.61
7742	$23^h44^m15^s$ $+10^h46^m01^s$	21.88	1659	SA(r)b	–	11.40	−20.30	0.65
7743	$23^h44^m21^s$ $+09^h56^m02^s$	18.69	1684	(R)SB(s)0+	–	11.31	−20.05	0.81
UGC4872	$09^h15^m01^s$ $+40^h02^m11^s$	112.20	8211	SBb	E	13.73	−21.52	0.74
UGC5666	$10^h28^m23^s$ $+68^h24^m43^s$	4.00	46	SAB(s)m	I	9.69	−18.32	0.33

Table B2. Lists exposure dates, exposure lengths, and the limiting surface brightness level which we reach in our observations.

NGC	Exp. date (mm/dd/yy)	Exp. length (s x n)	SBmin (mag arcsec^{-2})
M49(4472)	13/03/13	300 × 11	29.3
M51(5194/5195)	21/04/12	300 × 3	29.9
M59(4621)	24/05/12	300 × 10	29.1
M60(4649)	13/03/13	300 × 12	28.6
M63(5055)	29/01/11	300 × 16	29.5
M65(3623)	12/02/13	300 × 12	29.1
M66(3627)	13/03/13	300 × 12	29.6
M74(628)	22/10/11	300 × 31	29.7
M81(3031)	04/12/11	300 × 6	29.2
M82(3034)	18/10/12	300 × 4	28.7
M83(5236)	20/05/12	300 × 12	28.2
M86(4406)	09/06/13	300 × 5	28.1
M87(4486)	13/03/13	300 × 11	29.0
M90(4569)	22/04/14	300 × 17	28.9
M94(4736)	13/03/13	300 × 7	28.9
M95(3351)	08/02/11	300 × 5	28.6
M96(3368)	16/01/13	300 × 10	29.9
M101(5457)	11/06/13	300 × 8	29.7
M104(4594)	07/02/13	300 × 14	29.2
M105(3379)	07/02/13	300 × 12	29.1
M106(4258)	03/05/11	300 × 9	27.0
M108(3556)	27/05/14	300 × 6	28.6
M109(3992)	09/06/13	300 × 11	28.8
M110(205)	20/10/11	300 × 8	28.4
125	22/10/11	300 × 3	28.0
128	22/10/11	300 × 9	28.1
247	08/10/12	300 × 9	28.9

Table B2 – *continued*

NGC	Exp. date (mm/dd/yy)	Exp. length (s x n)	SBmin (mag arcsec^{-2})
278	07/10/16	100 × 6	28.4
467	16/10/12	300 × 12	28.0
470	16/10/12	300 × 12	28.3
474	16/10/12	300 × 12	28.9
509	19/10/12	300 × 11	28.6
518	30/11/11	300 × 4	28.5
520	27/09/16	300 × 10	28.4
524	30/11/11	300 × 4	28.3
525	30/11/11	300 × 4	27.6
530	18/10/12	300 × 11	28.5
532	30/11/11	300 × 4	28.2
596	11/12/12	300 × 11	28.9
636	11/12/12	300 × 10	29.6
661	19/10/12	300 × 12	29.1
672	11/12/12	300 × 13	29.2
720	27/10/11	300 × 13	29.9
772	18/10/12	300 × 12	29.0
891	04/09/11	300 × 11	28.2
925	07/10/16	300 × 12	28.8
1023	18/10/12	300 × 6	29.4
1055	20/12/12	300 × 10	28.3
1084	14/09/12	600 × 3	28.6
1289	20/11/12	300 × 9	28.7
1400	10/10/16	300 × 12	28.4
1407	10/10/16	300 × 12	28.2
2403	11/12/12	300 × 13	30.1
2481	16/01/13	300 × 12	28.4
2549	16/01/13	300 × 12	28.6
2683	01/01/14	300 × 12	29.3

Table B2 *– continued*

NGC	Exp. date (mm/dd/yy)	Exp. length (s x *n*)	SBmin (mag arcsec^{-2})
2685	30/11/11	300 × 7	28.3
2768	30/11/11	300 × 6	28.9
2782	20/11/12	300 × 7	28.2
2903	20/12/12	300 × 13	29.4
3032	30/11/11	300 × 10	28.5
3079	29/03/14	300 × 196	28.8
3115	20/05/12	300 × 7	29.4
3156	04/12/11	300 × 11	28.1
3384	03/05/11	300 × 18	28.9
3389	03/05/11	300 × 18	28.6
3521	07/02/13	300 × 12	29.7
3628	11/12/12	300 × 11	29.6
4038	24/02/14	300 × 49	28.5
4096	29/03/14	300 × 13	29.2
4206	22/04/12	300 × 11	28.5
4214	22/03/12	300 × 18	29.1
4216	22/04/12	300 × 11	29.1
4222	22/04/12	300 × 11	28.6
4244	14/04/13	300 × 12	28.9
4302	14/04/15	300 × 5	28.7
4395	06/06/15	300 × 17	29.3
4429	13/04/15	300 × 3	28.8
4449	31/05/11	300 × 35	28.9
4469	11/04/13	300 × 14	28.4
4517	29/05/14	300 × 16	28.5
4550	03/06/14	300 × 15	28.7
4551	03/06/14	300 × 15	28.7
4565	14/05/12	300 × 18	30.0
4631	14/04/13	300 × 12	29.8
4638	24/05/12	300 × 10	29.1
4697	22/02/15	300 × 2	29.1
4710	11/04/13	300 × 15	28.6
4754	18/05/12	300 × 7	28.1
4762	18/05/12	300 × 7	28.9
4866	12/02/13	300 × 12	29.2
5170	25/02/14	300 × 22	29.5
5576	20/04/12	300 × 21	29.4
5577	20/04/12	300 × 21	28.2
5713	03/06/11	300 × 10	28.5
5719	03/06/11	300 × 10	28.3
5746	20/05/12	300 × 9	28.9
5806	11/04/13	300 × 10	28.5
5811	11/04/13	300 × 10	28.2
5813	11/04/13	300 × 10	28.4
5814	11/04/13	300 × 10	28.4
5866	20/05/12	300 × 7	29.0
5907	09/06/13	300 × 13	29.0
6239	08/10/12	300 × 4	28.4
6340	11/06/13	300 × 9	28.1
6643	20/05/12	300 × 5	28.0
6946	21/09/11	300 × 14	28.4
7052	06/09/16	300 × 6	28.5
7217	29/08/16	300 × 12	28.6
7280	19/10/12	300 × 8	28.6
7331	21/08/12	600 × 8	28.4
7332	11/06/13	300 × 8	28.1
7463	14/09/12	600 × 6	28.1
7465	14/09/12	600 × 6	27.7
7479	17/09/12	600 × 6	28.8
7742	14/09/12	600 × 7	29.2
7743	14/09/12	600 × 7	28.3
UGC4872	16/10/12	300 × 9	26.9
UGC5666	16/01/13	300 × 12	28.7

Table B3. Lists our envelope diameter measurements (at the 28 mag arcsec^{-2} isophote) for each galaxy in arc-minutes and kpc, along with the envelope shape for each envelope.

NGC	Diameter (arcmin)	Diameter (kpc)	Envelope shape
M49(4472)	41.5 ± 1.7	200.8 ± 8.4	Round
M51(5194/5195)	26.8 ± 0.9	66.8 ± 2.1	Disturbed
M59(4621)	17.0 ± 0.9	72.9 ± 3.9	Round
M60(4649)	14.6 ± 0.5	72.6 ± 2.5	Round
M63(5055)	38.1 ± 1.2	100.2 ± 3.0	Oval
M65(3623)	12.0 ± 0.2	44.9 ± 0.9	Slightly boxy
M66(3627)	22.4 ± 0.5	74.8 ± 1.6	Oval
M74(628)	13.9 ± 0.1	40.9 ± 0.3	Round
M81(3031)	33.6 ± 0.8	35.2 ± 0.8	Oval
M82(3034)	41.3 ± 1.6	43.5 ± 1.7	Slightly oval
M83(5236)	22.9 ± 0.5	32.7 ± 0.7	Round
M86(4406)	25.8 ± 1.1	130.4 ± 5.5	Round
M87(4486)	41.8 ± 2.4	204.0 ± 11.5	Oval
M90(4569)	16.7 ± 0.7	57.7 ± 2.4	Oval
M94(4736)	23.5 ± 0.3	30.0 ± 0.4	Round
M95(3351)	11.7 ± 0.6	33.8 ± 1.7	Oval
M96(3368)	14.2 ± 0.1	40.4 ± 0.2	Oval
M101(5457)	32.7 ± 0.6	67.6 ± 1.2	Round
M104(4594)	30.8 ± 1.2	77.0 ± 3.0	Round
M105(3379)	19.5 ± 0.7	64.1 ± 2.4	Round
M106(4258)	–	–	Slightly diamond
M108(3556)	22.3 ± 0.5	63.6 ± 1.3	Oval
M109(3992)	10.7 ± 0.4	79.0 ± 2.6	Oval
M110(205)	36.0 ± 2.3	8.4 ± 0.5	Slight parallelogram
125	3.6 ± 0.3	66.3 ± 6.2	Circular
128	7.6 ± 0.7	99.6 ± 9.3	Oval
247	28.3 ± 0.7	30.5 ± 0.8	Discy
278	7.0 ± 0.3	36.1 ± 1.4	Circular
467	6.8 ± 0.2	116.3 ± 3.1	Circular disturbed
470	4.2 ± 0.2	59.3 ± 2.9	Oval
474	7.9 ± 0.6	62.9 ± 5.0	Circular disturbed
509	2.3 ± 0.1	21.8 ± 1.2	Oval
518	3.4 ± 0.2	38.6 ± 1.8	Oval
520	6.0 ± 0.2	31.0 ± 0.8	Disturbed
524	13.7 ± 0.4	129.6 ± 3.7	Circular
525	–	–	Diamond
530	2.0 ± 0.1	41.8 ± 2.4	Oval
532	8.0 ± 0.4	80.2 ± 4.0	Oval
596	15.7 ± 0.7	98.2 ± 4.1	Circular
636	9.2 ± 0.4	79.1 ± 3.3	Circular
661	5.9 ± 0.3	64.0 ± 3.2	Round
672	10.2 ± 0.5	21.4 ± 1.0	Oval
720	19.7 ± 0.9	156.8 ± 6.8	Boxy
772	14.8 ± 0.7	109.9 ± 5.2	Oval disturbed
891	13.1 ± 0.2	37.4 ± 0.6	Diamond
925	12.3 ± 0.3	32.8 ± 0.8	Oval
1023	18.0 ± 0.5	50.1 ± 1.4	Boxy hexagon
1055	20.2 ± 0.9	113.4 ± 5.0	Boxy hexagon
1084	12.1 ± 0.7	54.3 ± 3.3	Round
1289	6.4 ± 0.5	56.0 ± 4.4	Round
1400	10.1 ± 0.7	76.9 ± 5.0	Round
1407	17.6 ± 1.0	146.0 ± 8.6	Round
2403	26.4 ± 0.5	24.6 ± 0.5	Oval
2481	3.2 ± 0.1	29.1 ± 1.1	Oval
2549	6.2 ± 0.1	22.5 ± 0.3	Oval
2683	11.4 ± 0.4	31.2 ± 1.0	Diamond
2685	7.1 ± 0.3	26.1 ± 1.1	Slightly diamond
2768	14.9 ± 0.5	95.8 ± 3.5	Round
2782	7.3 ± 0.2	36.3 ± 1.2	Round disturbed
2903	24.1 ± 0.6	65.3 ± 1.7	Discy

Table B3 – *continued*

NGC	Diameter (arcmin)	Diameter (kpc)	Envelope shape
3032	4.3 ± 0.2	24.8 ± 1.0	Round
3079	11.2 ± 0.5	53.8 ± 2.2	Oval
3115	24.8 ± 1.0	69.7 ± 2.9	Oval
3156	5.0 ± 0.3	32.2 ± 1.8	Oval
3384	12.3 ± 0.1	33.8 ± 0.2	Oval
3389	4.7 ± 0.1	26.6 ± 0.8	Oval
3521	22.4 ± 0.4	80.6 ± 1.4	Oval/diamond
3628	20.7 ± 0.2	65.1 ± 0.5	Boxy
4038	16.1 ± 1.6	114.7 ± 11.6	Disturbed with antennae
4096	13.1 ± 0.3	45.7 ± 1.1	Discy
4206	6.8 ± 0.2	37.3 ± 1.0	Oval
4214	11.6 ± 0.2	10.0 ± 0.1	Round
4216	10.7 ± 0.1	42.8 ± 0.3	Boxy
4222	6.9 ± 0.3	39.8 ± 1.6	Discy
4244	22.1 ± 0.5	27.9 ± 0.7	Discy
4302	11.0 ± 0.2	45.8 ± 0.9	Oval
4395	16.9 ± 0.3	23.4 ± 0.4	Round
4429	12.1 ± 0.4	45.8 ± 1.4	Oval
4449	21.3 ± 0.7	26.4 ± 0.9	Round
4469	10.8 ± 0.5	52.8 ± 2.2	Oval
4517	18.5 ± 0.9	45.1 ± 2.1	Oval
4550	6.3 ± 0.3	27.8 ± 1.3	Diamond
4551	4.5 ± 0.3	21.2 ± 1.2	Round
4565	21.1 ± 0.6	74.1 ± 2.1	Diamond
4631	21.5 ± 0.4	46.0 ± 0.9	Boxy
4638	5.3 ± 0.3	26.7 ± 1.7	Round
4697	17.5 ± 0.7	62.1 ± 2.6	Round
4710	9.4 ± 0.4	46.0 ± 1.9	Diamond
4754	7.9 ± 0.6	36.7 ± 2.7	Oval
4762	14.9 ± 0.4	47.0 ± 1.2	Boxy
4866	8.0 ± 0.2	68.8 ± 1.8	Oval
5170	11.6 ± 0.2	98.7 ± 1.6	Boxy/diamond
5576	11.5 ± 0.4	84.0 ± 2.8	Round
5577	4.4 ± 0.2	24.9 ± 0.9	Discy
5713	4.8 ± 0.1	28.2 ± 0.8	Round
5719	7.0 ± 0.2	53.7 ± 1.6	Slightly diamond
5746	11.1 ± 0.4	87.0 ± 3.2	Oval
5806	7.3 ± 0.2	43.6 ± 1.2	Oval
5811	3.2 ± 0.1	22.7 ± 0.5	Oval
5813	16.5 ± 0.7	153.1 ± 6.5	Oval
5814	6.7 ± 0.4	305.8 ± 17.2	Oval
5866	9.1 ± 0.3	38.4 ± 1.1	Round/boxy
5907	15.5 ± 0.3	77.9 ± 1.7	Oval
6239	5.3 ± 0.3	37.6 ± 1.9	Disturbed
6340	11.5 ± 0.8	65.1 ± 4.4	Round
6643	5.5 ± 0.2	32.4 ± 1.4	Oval
6946	25.9 ± 0.5	50.7 ± 1.0	Round

Table B3 – *continued*

NGC	Diameter (arcmin)	Diameter (kpc)	Envelope shape
7052	7.8 ± 0.4	116.2 ± 6.2	Boxy
7217	11.0 ± 0.4	58.5 ± 1.9	Round
7280	3.4 ± 0.1	21.3 ± 0.8	Round
7331	14.7 ± 0.5	62.3 ± 1.9	Diamond
7332	5.2 ± 0.1	34.3 ± 1.0	Diamond
7463	6.4 ± 0.3	42.8 ± 1.9	Disturbed
7465	–	–	Round
7479	8.2 ± 0.4	71.8 ± 3.1	Oval
7742	4.7 ± 0.1	29.9 ± 0.6	Round
7743	8.5 ± 0.4	46.4 ± 2.0	Oval
UGC4872	–	–	Oval
UGC5666	16.7 ± 0.6	19.4 ± 0.7	Oval

[1]*Department of Physics & Astronomy, University of California Los Angeles, 430 Portola Plaza, Los Angeles, CA 90095, USA*
[2]*Central Astronomical Observatory, Russian Academy of Sciences, 65/1 Pulkovskoye chaussee, St Petersburg 196140, Russia*
[3]*Zentrum für Astronomie der Universität Heidelberg, Astronomisches Rechen-Institut, D-69120 Heidelberg, Germany*
[4]*Department of Astronomy, University of Texas at Austin, 2515 Speedway, Mail Stop C1400, Austin, TX 78712, USA*
[5]*Department of Physics, University of Arkansas, 825 West Dickson Street, Fayetteville, AR 72701, USA*
[6]*Wise Observatory, Tel Aviv University, 69978 Tel Aviv, Israel*
[7]*Department of Physics & Astronomy, University of California Riverside, Riverside, CA 92521, USA*
[8]*Department of Physics & Astronomy, University of California, Irvine, 4129 Frederick Reines Hall, Irvine, CA 92697, USA*
[9]*Department of Physics, Ludwig-Maximillians Universitat München, Schellingstrasse 4, D-80799 Munich, Germany*
[10]*Department of Physics, University of Surrey, Surrey GU2 7XH, UK*
[11]*Griffith Observatory, 2800 East Observatory Road, Los Angeles, CA 90027, USA*
[12]*Department of Physics and Astronomy, Johns Hopkins University, 3400 N. Charles Street, Baltimore, MD 21218, USA*
[13]*Department of Earth, Planetary & Space Sciences, 595 Charles Young Drive, University of California Los Angeles, CA 90095, USA*
[14]*NASA Jet Propulsion Laboratory, 4800 Oak Grove Drive, Pasadena, CA 91109, USA*
[15]*Department of Physics, The College of Wooster, 308 E. University Street, Wooster OH 44691, USA*

This paper has been typeset from a TEX/LATEX file prepared by the author.